

Supplemental Information

1. Experimental Section

Materials and synthesis

General information: Compound 1 and Compound 2 were according to the literature^[1], and the NMR spectra of Compound 2 are listed in Figure S1-2. Other reagents were purchased from Energy Chemical (Sun Chemical Technology (Shanghai) Co., Ltd.) or Bide Pharmatech Ltd. Unless otherwise stated, analytical grade solvents and commercially available reagents were used without further purification. SD-86 was characterized by ¹H NMR and ¹³C NMR spectra, which were recorded on an AVANCE NEO 600 MHz spectrometer at room temperature. The chemical shifts (δ) were given in part per million relatives to internal tetramethyl silane (TMS, 0 ppm for ¹H) and CDCl₃ (77.0 ppm for ¹³C). All chemical shifts (δ) were reported in ppm and coupling constants (J) in Hz. High-resolution mass spectrum (MALDI-TOF-MS) was determined using an autoflex max TOF Mass Spectrometer, peaks are given in m/z.

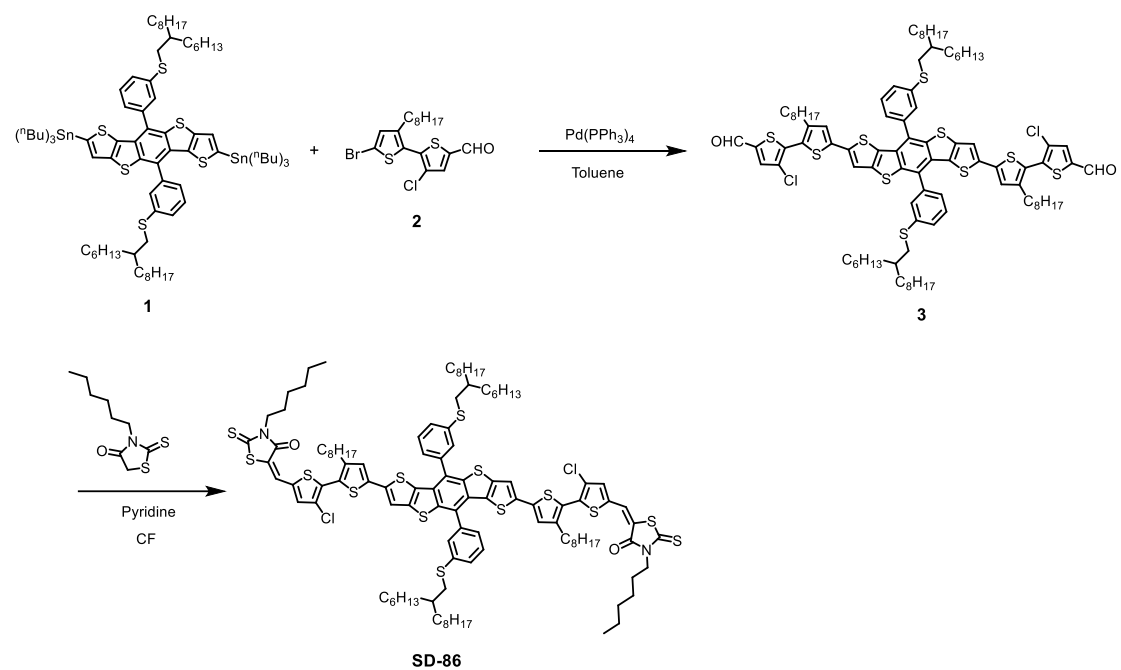
Synthesis of Compound 3: Compound 1 (200 mg, 0.129 mmol), Compound 2 (136 mg, 0.324 mmol), and Pd(PPh₃)₄ (15 mg, 0.014 mmol) were dissolved in deoxygenated toluene. The reaction mixture was refluxed for 12 h and then extracted with dichloromethane (DCM). The collected organic layer was dried over anhydrous MgSO₄. After removal of the solvent under reduced pressure, the residue was purified by silica gel chromatography (petroleumether (PE)/chloroform (CF), v/v = 1:1) as eluent and then recrystallized from methylalcohol to give a red product (119 mg, 56%). ¹H NMR (600 MHz, CDCl₃, δ /ppm) δ 9.84 (s, 2H), 7.66 (s, 2H), 7.61-7.58 (m, 6H), 7.45 (d, J = 6.6 Hz, 2H), 7.32 (s, 2H), 7.01 (s, 2H), 3.00 (m, 4H), 2.62 (t, J = 7.8 Hz, 4H), 1.74-1.70 (m, 2H), 1.62-1.57 (m, 4H), 1.46-1.36 (m, 8H), 1.31-1.20 (m, 60H), 0.88-0.82 (m, 18H). ¹³C NMR (151 MHz, CDCl₃, δ /ppm) δ 181.75, 145.37, 141.41, 140.99, 139.94, 139.82,

139.50, 138.98, 138.47, 137.80, 136.38, 132.80, 129.86, 129.57, 128.85, 126.24, 126.24, 125.48, 124.40, 116.83, 38.33, 38.31, 37.61, 33.26, 33.22, 31.92, 31.86, 31.84, 31.82, 30.51, 29.98, 29.93, 29.72, 29.64, 29.60, 29.57, 29.44, 29.37, 29.34, 29.34, 29.33, 29.23, 26.62, 26.60, 26.57, 26.55, 26.53, 22.70, 22.67, 14.13 (Note: some peaks in ^{13}C NMR spectrum overlap).

Synthesis of SD-86: Under nitrogen atmosphere, a mixture solution of Compound 3 (80 mg, 0.048 mmol), 3-hexyl-2-thioxothiazolidin-4-one (84 mg, 0.389 mmol), piperidine (0.3 mL), and CF (10 mL) was added to a 25 mL round bottom flask and then refluxed for 12 h. After cooling to room temperature, the mixture was poured into methanol and then filtered. The residue was purified by column chromatography on silica gel using a mixture solvent as eluent (PE/CF, v/v = 1:2) to give a black purple solid (70 mg, 70%). ^1H NMR (600 MHz, CDCl_3 , δ /ppm) δ 7.70 (s, 2H), 7.61-7.57 (m, 6H), 7.45 (d, J = 4.5 Hz, 2H), 7.31 (s, 2H), 7.28 (s, 2H), 7.00 (s, 2H), 4.10 (t, J = 4.2 Hz, 4H), 3.00 (d, J = 4.8 Hz, 4H), 2.65 (t, J = 5.2 Hz, 4H), 1.74-1.67 (m, 6H), 1.63-1.58 (m, 4H), 1.46-1.17 (m, 80H), 0.89-0.83 (m, 24H). ^{13}C NMR (151 MHz, CDCl_3 , δ /ppm) δ 191.59, 167.38, 145.09, 141.40, 140.02, 139.81, 139.47, 138.77, 137.79, 136.47, 135.53, 133.60, 132.72, 129.84, 129.58, 129.52, 128.85, 128.82, 126.28, 126.25, 124.57, 123.14, 122.76, 116.70, 44.94, 38.34, 38.31, 37.60, 33.24, 33.21, 33.19, 31.91, 31.88, 31.84, 31.81, 31.31, 30.57, 29.97, 29.92, 29.70, 29.63, 29.59, 29.56, 29.51, 29.37, 29.33, 29.29, 26.92, 26.61, 26.59, 26.56, 26.54, 26.52, 26.43, 22.69, 22.66, 22.50, 14.14, 14.11, 14.40 (Note: some peaks in ^{13}C NMR spectrum overlap).

MS (MALDI-TOF) m/z Calcd. For $\text{C}_{110}\text{H}_{142}\text{Cl}_2\text{N}_2\text{O}_2\text{S}_{14}$: 2042.6536, Found 2042.5479.

Synthesis of SD86



Scheme S1. The synthetic route of SD-86.

General Information: NMR spectra were measured on Bruker AVANCE 600 MHz spectrometer with *d* chloroform as the solvent. The chemical shifts were reported as δ value (ppm) relative to an internal tetramethylsilane (TMS) standard. Mass spectra (MALDI-TOF-MS) were determined using Bruker BIFLEX III Mass Spectrometer and AB SCIEX 5800 Mass Spectrometer.

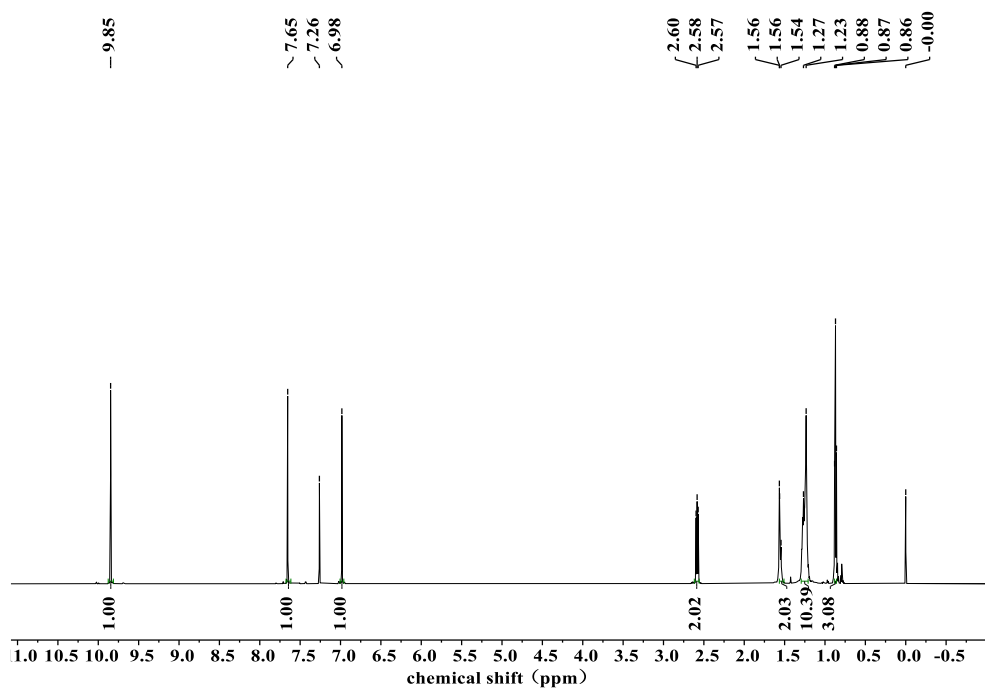


Figure S1. ^1H NMR spectrum of Compound 2.

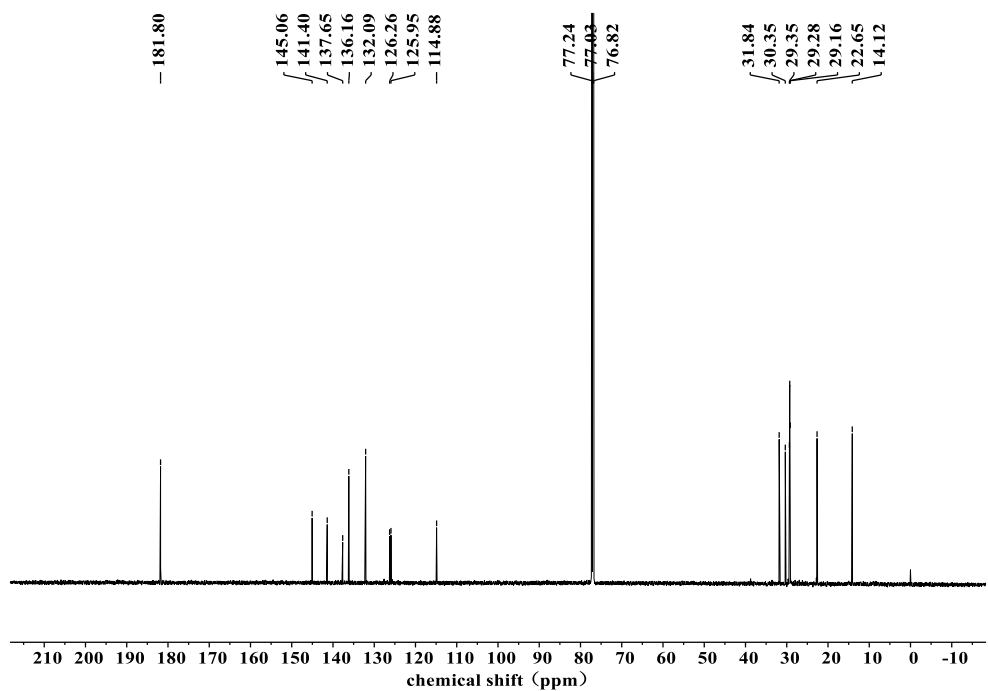


Figure S2. ^{13}C NMR spectrum of Compound 2.

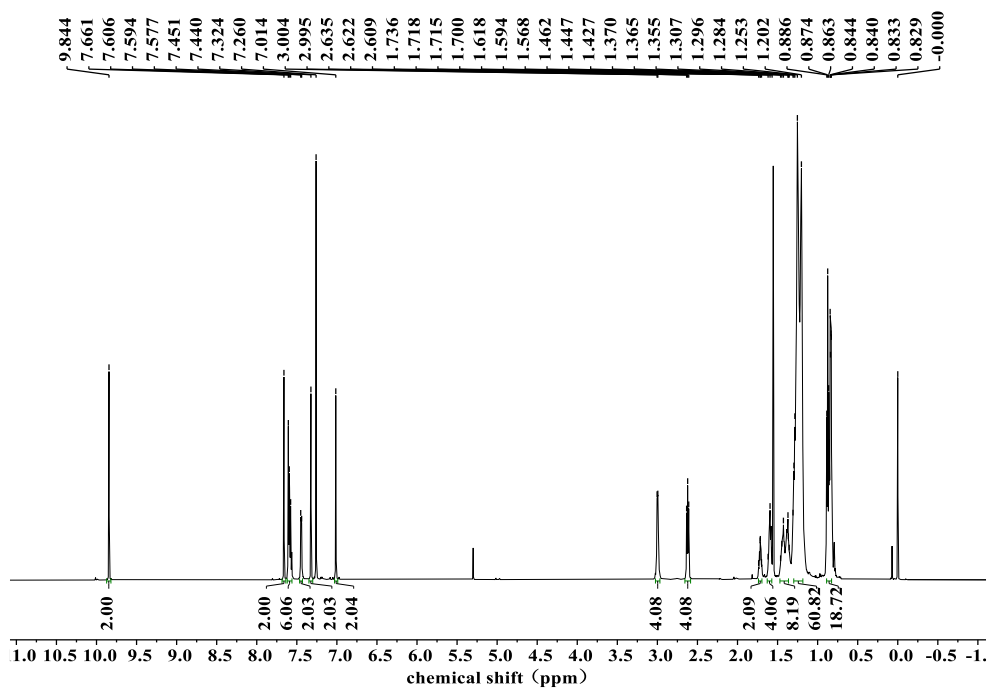


Figure S3. ^1H NMR spectrum of Compound 3.

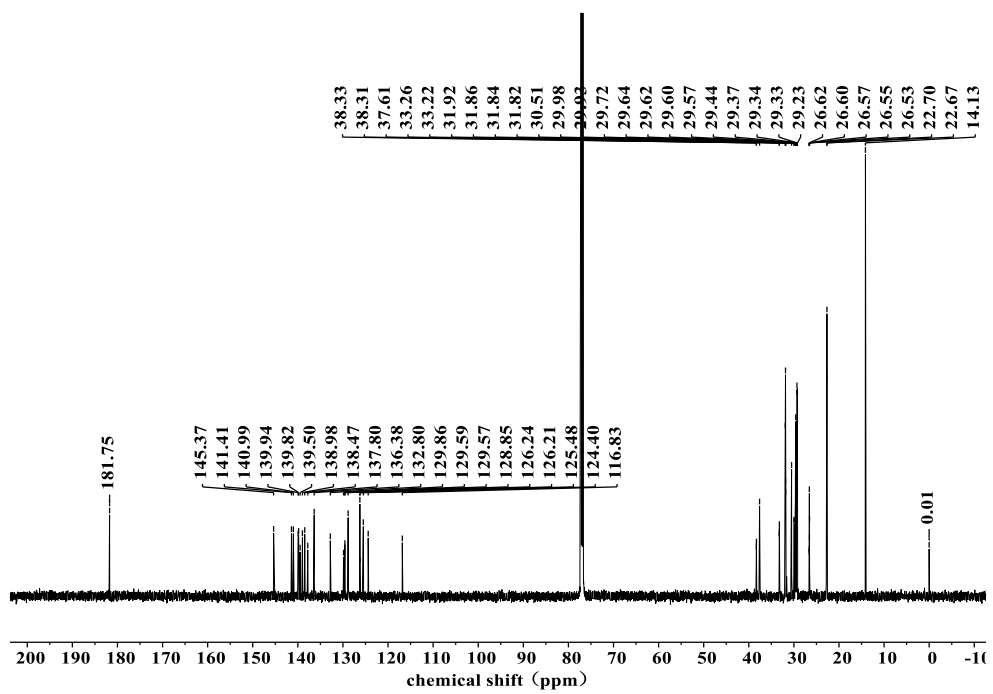


Figure S4. ^{13}C NMR spectrum of Compound 2.

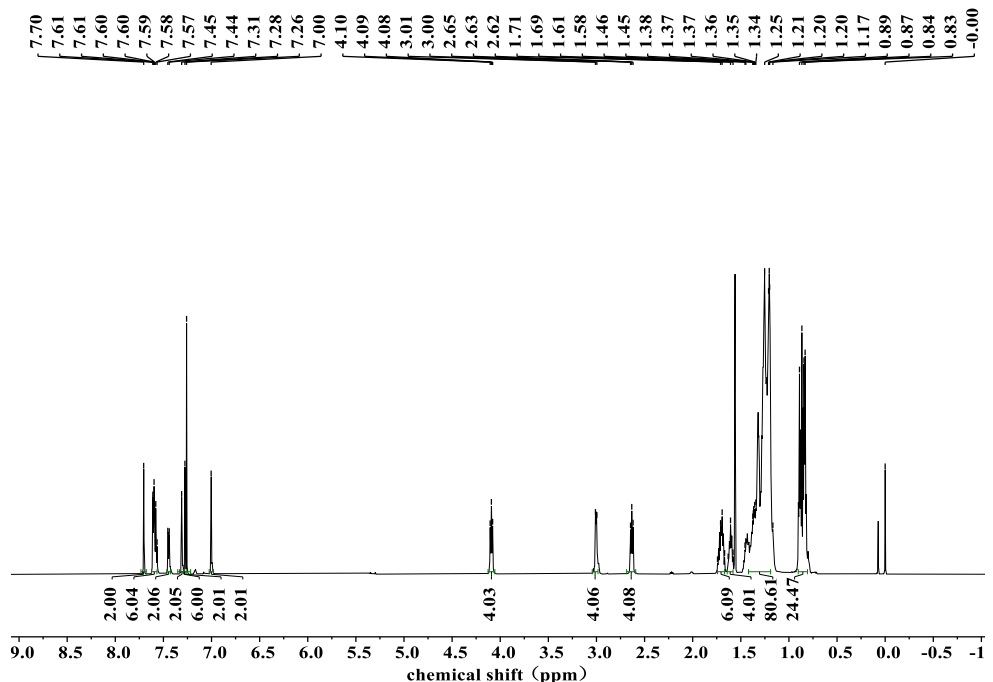


Figure S5. ^1H NMR spectrum of SD-86.

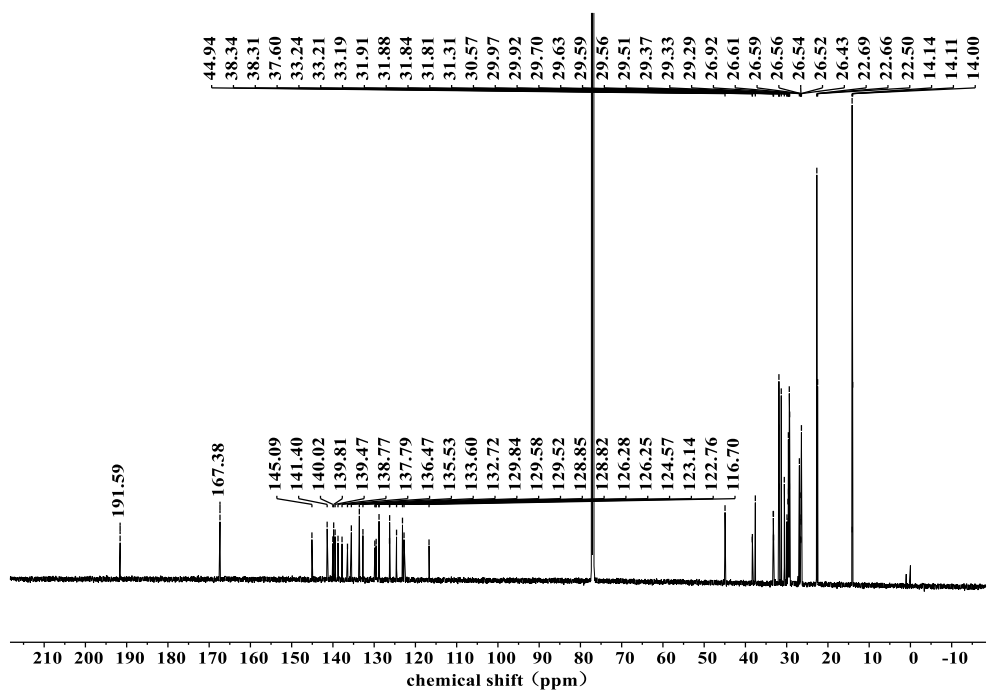


Figure S6. ^{13}C NMR spectrum of SD-86.

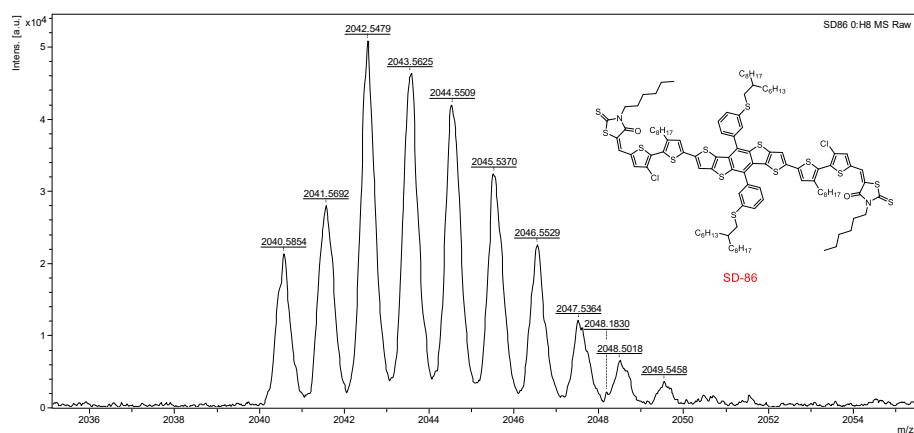


Figure S7. MALDI-TOF spectrum of SD-86.

Electrochemical characterizations: Electrochemical properties were studied by cyclic voltammetry (CV), which was performed on a CS350H electrochemical workstation with a three-electrode system in a 0.1 M Bu₄NPF₆ acetonitrile solution at a scan rate of 100 mV s⁻¹. A glassy carbon disc coated with sample film was used as the working electrode. A Pt wire was used as the counter electrode and Ag/AgCl was used as the reference electrode. The HOMO/LUMO energy levels ($E_{\text{HOMO}}/E_{\text{LUMO}}$) can be calculated from onset oxidation/reduction potentials ($\phi_{\text{ox}}/\phi_{\text{red}}$) in the cyclic voltammograms according to the equations of $E_{\text{HOMO}}/E_{\text{LUMO}} = -e(\phi_{\text{ox}}/\phi_{\text{Red}} + 4.8 - \phi_{\text{Fe/Fe}^+})$ (eV) (eV), where $\phi_{\text{Fe/Fc}^+}$ is the redox potential of ferrocene/ferrocenium (Fe/Fc⁺) couple in the electrochemical measurement system, and the energy level of Fe/Fc⁺ was taken as 4.8 eV below vacuum.

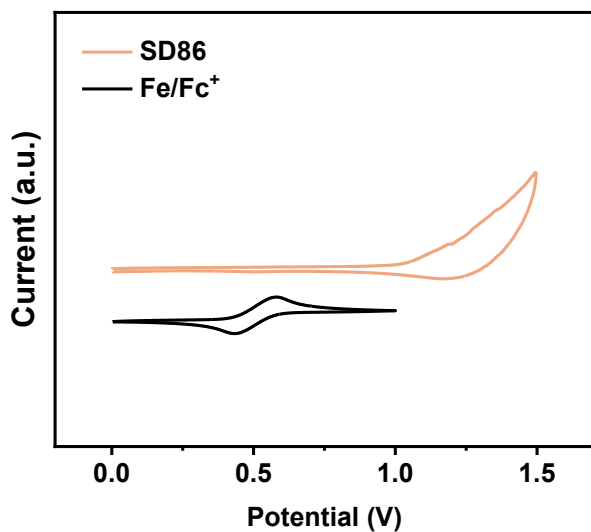


Figure S8. Cyclic voltammetry curves of the SD86 neat film.

Optical measurements and simulations: Ultraviolet-visible near-infrared (UV-vis-NIR) absorption spectra were recorded with a Perkin-Elmer Lambda 365 UV-Vis spectrophotometer from 300 nm to 1100 nm. The optical simulations were calculated by Fluxim Setfos software.

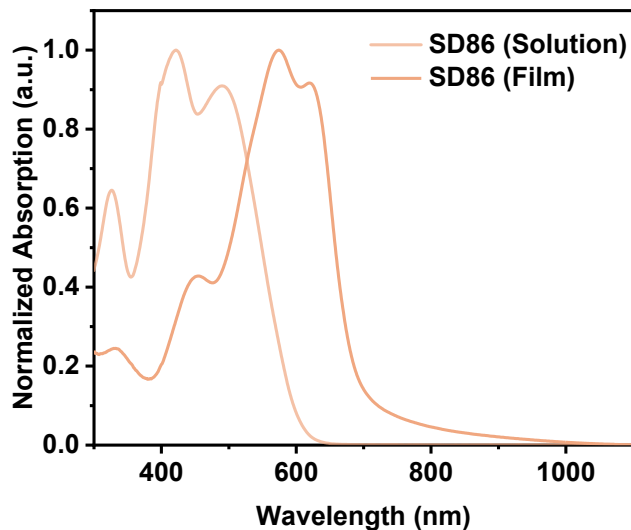


Figure S9. Normalized UV-vis absorption spectra of SD86 in chloroform solution and in the solid state.

Table S1. Optical and electrochemical properties of MPhS-C2, SD86, and BTP-eC9.

Materials	$\lambda_{\text{max,sol}}$ [nm]	$\lambda_{\text{max,film}}$ [nm]	$\lambda_{\text{onset,film}}$ [nm]	E_g^{a} [eV]	LUMO/HOMO ^b [eV]
MPhS-C2	522	569	705	1.76	-3.45/-5.35
SD86	422	575	719	1.72	-3.68/-5.40
BTP-eC9	746	829	912	1.36	-3.98/-5.62

^a calculated from the absorption onset of the films.

^b estimated from the reduction/oxidation onset of the CV curves.

Grazing incidence wide-angle X-ray scattering (GIWAXS) characterization: The grazing incidence X-ray scattering (GIWAXS) measurement was carried out with a Xeuss 2.0 SAXS/WAXS laboratory beamline using a Cu X-ray source (8.05 keV, 1.54 Å) and a Pilatus3R 300K detector. The incident angle was 0.15°. The samples for the GIWAXS measurements were fabricated on silicon substrates.

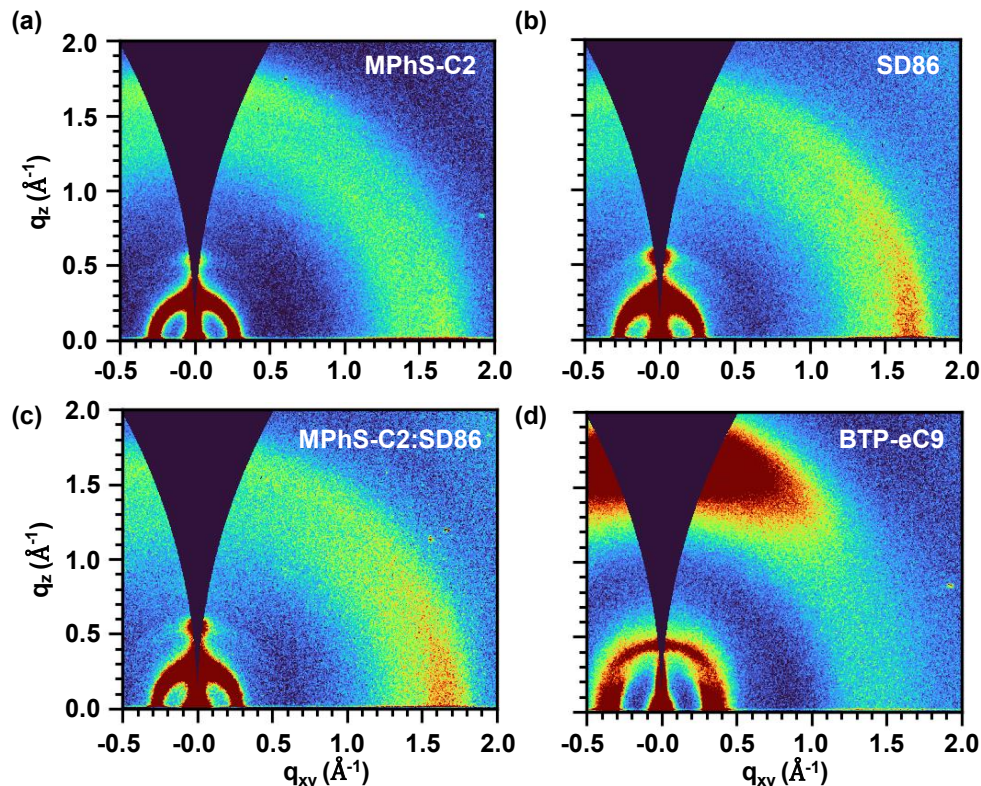


Figure S10. The 2D-GIWAXS patterns of (a) MPhS-C2, (b) SD86, (c) MPhS-C2: SD86 and (d) BTP-eC9 thin-films.

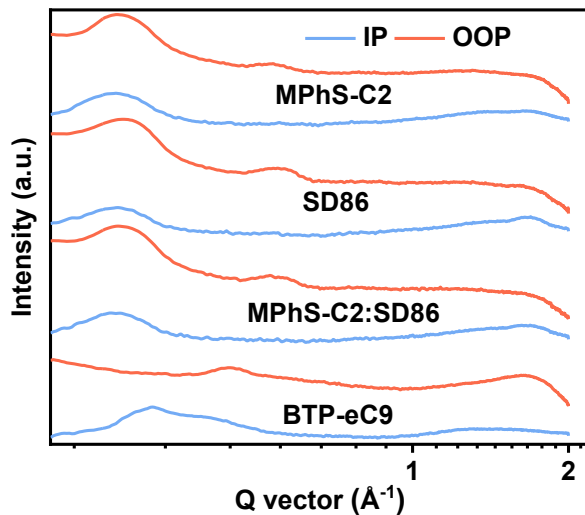


Figure S11. The corresponding in-plane (IP) and out-of-plane (OOP) line-cuts of the small molecule films acquired at a critical incident angle of 0.15°.

Table S2. Investigations of the morphology parameters extracted from the GIWAXS measurements of the neat MPhS-C2, SD86, and MPhS-C2:SD86 films.

Neat films	Out-of-plane (100)		In-plane (010)			
	q (Å⁻¹)	d-spacing (Å)	q (Å⁻¹)	d-spacing (Å)	FWHM (Å⁻¹)	L _c (Å)
MPhS-C2	0.26	24.15	1.65	3.81	1.12	5.61
SD86	0.28	22.43	1.68	3.74	0.32	19.63
MPhS-C2:SD86	0.27	23.26	1.67	3.76	0.37	16.97
BTP-eC9	0.44	14.27	/	/	/	/

Contact Angle Measurements and Interfacial Tension Calculation: The contact angles of two small molecule donors (MPhS-C2 and SD86) and small molecule acceptor BTP-eC9 were measured using a Contact Angle Analyzer. The contact angles of two different solvents (water and ethylene glycol (EG)) on the neat films were used to calculate the surface tension of each film by the Wu model. The interfacial tension between each acceptor and donor was calculated with the surface tensions of the materials.

Table S3. Investigations of the contact angles and surface energy values of MPhS-C2, SD86, and BTP-eC9.

Materials	Contact		Surface energy [mN m ⁻¹]	Relative χ	
	Water	Ethylene glycol		(w MPhS-C2)	(w BTP-eC9)
MPhS-C2	105.2 (105.2±0.05)	75.3 (75.3±0.03)	49.71 (49.71±0.06)	/	/
	104.7 (104.7±0.04)	75.0 (75.0±0.06)	48.81 (48.81±0.05)	0.004 <i>K</i>	0. 303 <i>K</i>
BTP-eC9	98.2 (98.2±0.03)	65.5 (65.5±0.04)	56.83 (56.83±0.06)	0. 240 <i>K</i>	/

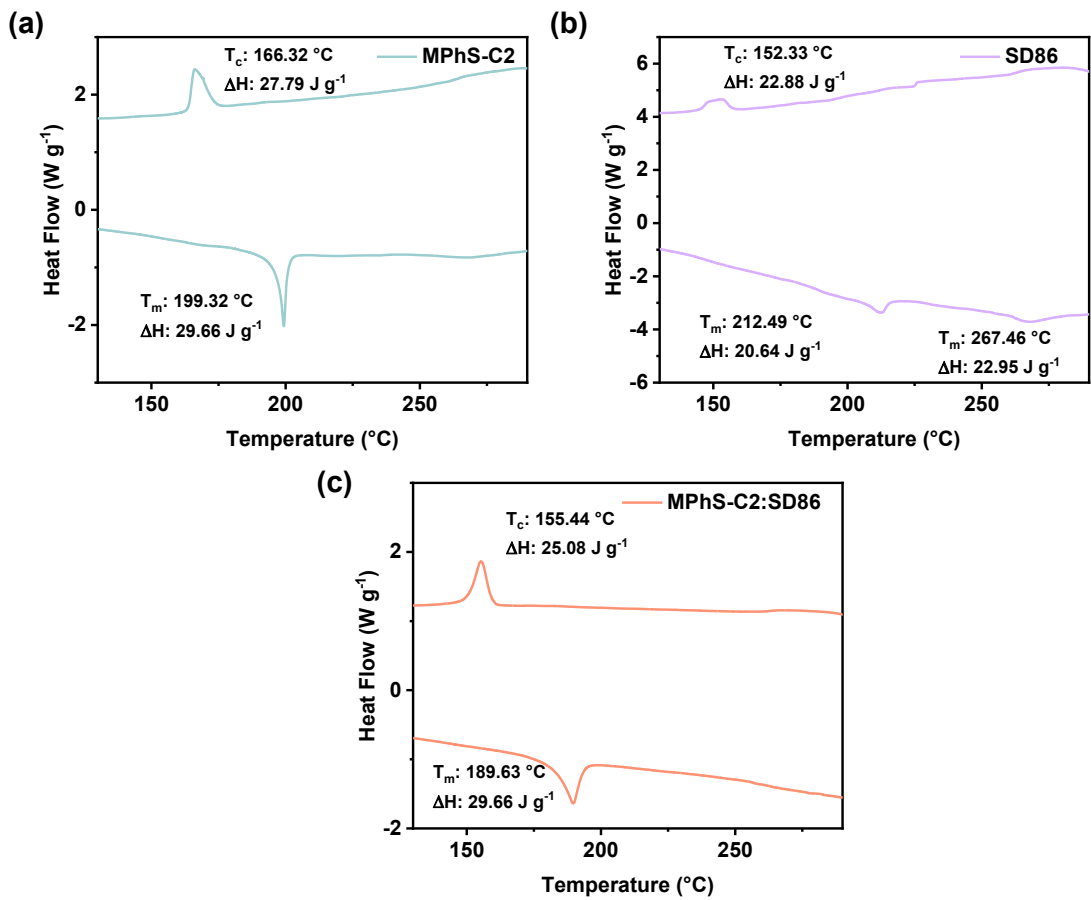


Figure S12. The DSC curves of (a) MPhS-C2 and (b) SD86 as well as the (c) MPhS-C2:SD86 (80:20, wt%) with a heating rate of $10\text{ }^\circ\text{C min}$ under nitrogen atmosphere.

Space charge limited current (SCLC) measurements: Single carrier devices were fabricated, and the dark current-voltage characteristics were measured and analyzed in the space charge limited (SCL) regime following the references. The structure of hole-only devices was Glass/ITO/PEDOT:PSS/Active layer/MoO₃ (10 nm)/Ag (100 nm). For the electron-only devices, the structure was Glass/ITO/ZnO/Active layer/PNDIT-F3N/Ag (100 nm), where the Ag was evaporated. The *J-V* characteristics of both hole-only and electron-only diodes can be excellently fit to the Mott-Gurney relation for space charge limited current: $J_{SCL} = \frac{9}{8} \varepsilon_0 \varepsilon_r \mu \frac{V_{in}^2}{L^3} \exp\left(\frac{0.89 \times \beta}{\sqrt{L}} \sqrt{V_{in}}\right)$, Where J_{SCL} is the current density, ε_0 is the permittivity of free space, ε_r is the relative dielectric constant of the active layer, μ is the charge carrier mobility, β is the field activation factor, L is the thickness of the device and V_{in} is the voltage dropped across the sample.

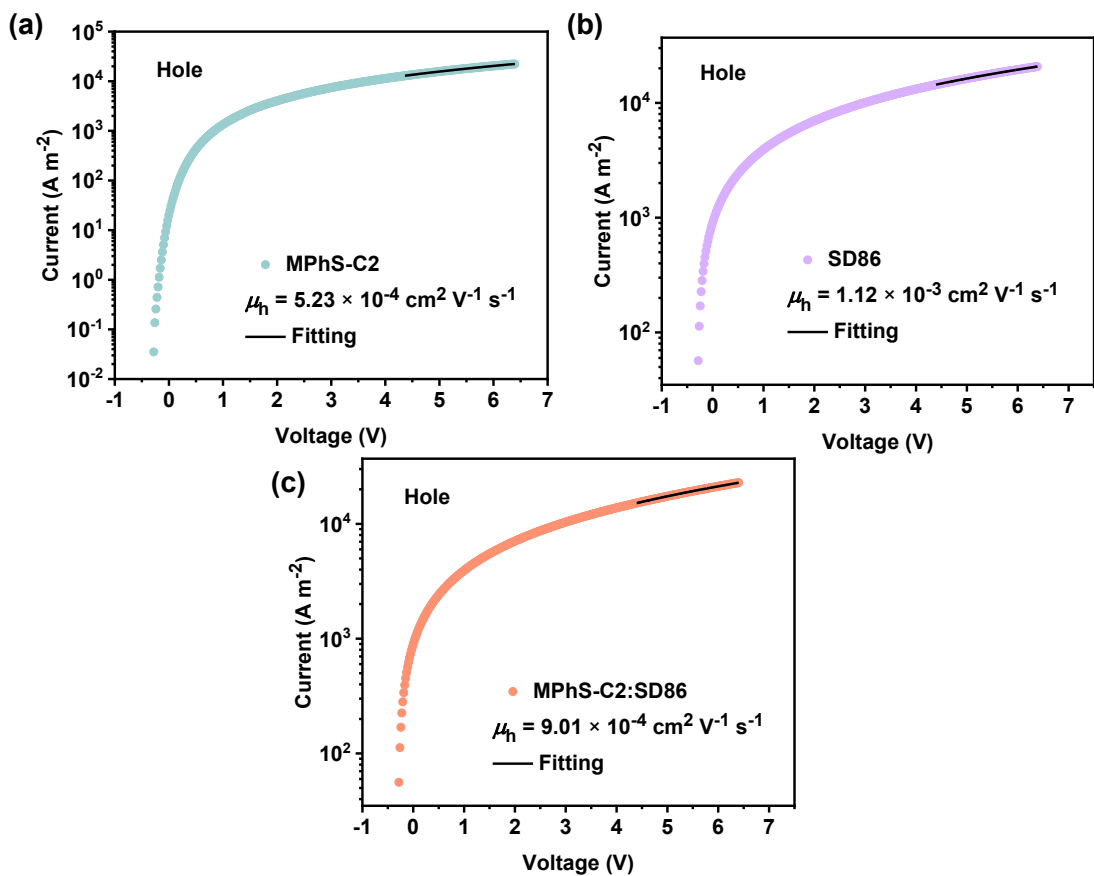


Figure S13. The hole mobilities of pristine (a) MPhS-C2 and (b) SD86 small molecule donor films as well as the (c) MPhS-C2:SD86 (80:20, wt%), measured using the space-charge-limited-current approach.

Device Fabrication and Testing

Solar cells were fabricated in a conventional device configuration of ITO/PEDOT:PSS (40nm)/Active layer/PNDIT-F3N/Ag. Pre-patterned ITO-coated glass substrates (purchased from South China Science & Technology Company Limited) washed with methylbenzene, deionized water, acetone, and isopropyl alcohol in an ultrasonic bath for 15 min each. After blow-drying with high-purity nitrogen, All ITO substrates are cleaned in an ultraviolet ozone cleaning system for 15 minutes. Subsequently, a thin layer of PEDOT: PSS (Xi'an Polymer Light Technology Corp 4083) was deposited through spin-coating at 4500 rpm for 30 s on pre-cleaned ITO-coated glass from a PEDOT: PSS aqueous solution and annealed at 150 °C for 15 min in atmospheric air. The MPhS-C2: acceptor blends (1.7:1 weight ratio) were dissolved in chloroform solution with 0.25% additive of 1,8-diiodooctane (DIO). The total concentration of blend solutions was 18 mg mL⁻¹ for all blends and stirred at 45 °C for 3 hours. The blend solution was spin-coated at 3200 rpm for 30 s. The blend was thermally annealed at 115 °C for 7 min, and the solvent (CF) was further annealed for 60 s. The thickness optimal active layer measured by a Bruker Dektak XT stylus profilometer was about 130 nm. Then methanol solution of PNDIT-F3N at a concentration of 0.5 mg ml⁻¹ was spin-coated onto the active layer at 4000 rpm for 20s. Finally, the top argentum electrode of 100 nm thickness was thermally evaporated through a mask onto the cathode buffer layer under a vacuum of $\sim 5 \times 10^{-6}$ mbar. The typical active area of the investigated devices was 4.8 mm². The current-voltage characteristics of the solar cells were measured by a Keithley 2400 source meter unit under AM1.5G (100 mW cm⁻²) irradiation from a solar simulator (Enlitech model SS-X160R). Solar simulator illumination intensity was determined at 100 mW cm⁻² using a monocrystalline silicon reference cell with a KG5 filter. Short circuit currents under AM1.5G (100 mW cm⁻²) conditions were estimated from the spectral response and convolution with the solar spectrum. The forward scan was adopted to test the *J-V* curves, the scan step is 0.02 V and the delay time is 1 ms. The scan mode is sweep.

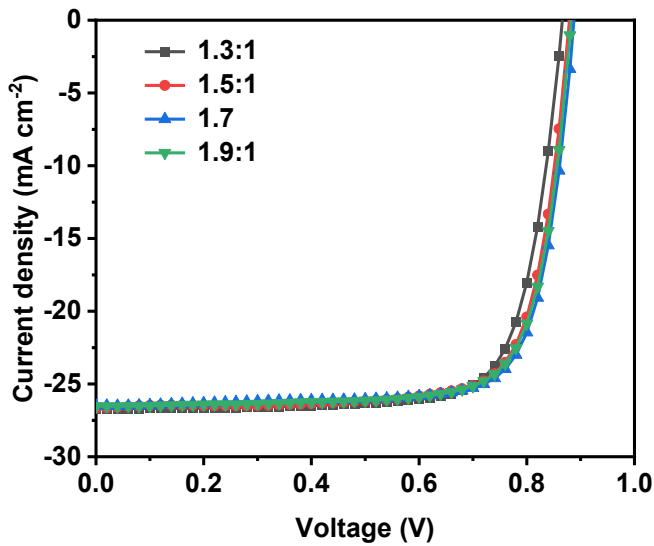


Figure S14. Relevant J - V curves of the ternary small molecule organic solar cells with different D/A ratios measured under the illumination of AM 1.5G at 100 mW cm^{-2} .

Table S4. Photovoltaic parameters of the MPhS-C2:SD86:BTP-eC9 devices with different D/A ratios, measured under the illumination of AM 1.5G at 100 mW cm^{-2} .

D/A ratios [%]	V_{OC} [V]	J_{SC} [mA cm $^{-2}$]	FF [%]	PCE ^a [%]
1.3:1	0.866 (0.862 ± 0.008)	26.72 (26.60 ± 0.25)	76.46 (76.30 ± 0.20)	17.69 (17.50 ± 0.10)
	0.879 (0.876 ± 0.006)	26.65 (26.55 ± 0.15)	76.70 (76.60 ± 0.25)	17.97 (17.75 ± 0.20)
1.5:1	0.887 (0.885 ± 0.005)	26.49 (26.30 ± 0.25)	77.55 (77.40 ± 0.30)	18.22 (18.05 ± 0.15)
	0.882 (0.880 ± 0.005)	26.53 (26.30 ± 0.30)	77.01 (76.85 ± 0.20)	18.02 (17.80 ± 0.20)
1.7:1				
1.9:1				

^aThe values in parenthesis are the average PCEs obtained from 30 devices.

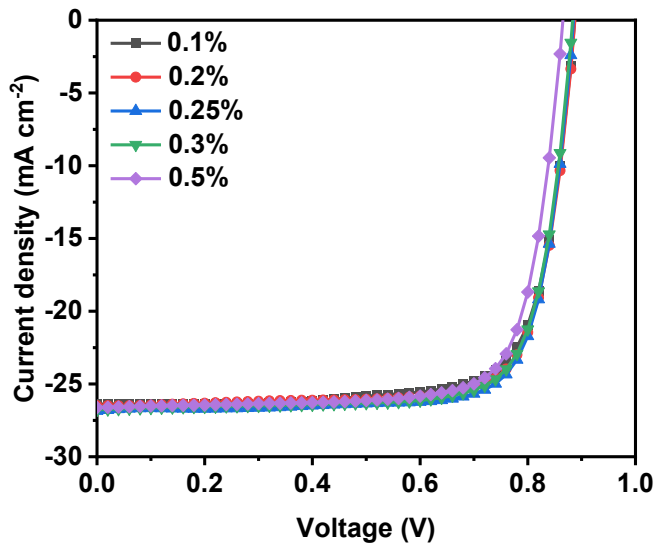


Figure S15. Relevant J - V curves of the ternary small molecule organic solar cells with different ratios of DIO measured under the illumination of AM 1.5G at 100 mW cm^{-2} .

Table S5. Photovoltaic parameters of the MPhS-C2:SD86:BTP-eC9 devices with different ratios of DIO, measured under the illumination of AM 1.5G at 100 mW cm^{-2} .

DIO ratios [%]	V_{OC} [V]	J_{SC} [mA cm $^{-2}$]	FF [%]	PCE ^a [%]
0.1	0.887 (0.883 ± 0.007)	26.38 (26.20 ± 0.20)	76.10 (75.95 ± 0.20)	17.81 (17.68 ± 0.12)
0.2	0.887 (0.885 ± 0.005)	26.49 (26.30 ± 0.25)	77.55 (77.40 ± 0.30)	18.22 (18.05 ± 0.15)
0.25	0.885 (0.878 ± 0.008)	26.85 (26.70 ± 0.30)	77.89 (77.75 ± 0.30)	18.51 (18.20 ± 0.25)
0.3	0.883 (0.880 ± 0.005)	26.77 (26.70 ± 0.15)	77.25 (77.05 ± 0.25)	18.26 (18.15 ± 0.10)
0.5	0.865 (0.862 ± 0.006)	26.62 (26.55 ± 0.10)	76.95 (76.85 ± 0.15)	17.72 (17.60 ± 0.10)

^aThe values in parenthesis are the average PCEs obtained from 30 devices.

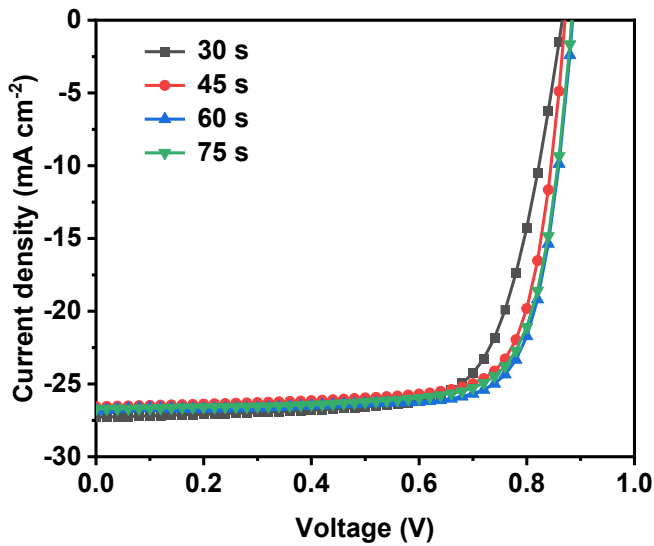


Figure S16. Relevant J - V curves of the ternary small molecule organic solar cells with different SVA time measured under the illumination of AM 1.5G at 100 mW cm^{-2} .

Table S6. Photovoltaic parameters of the MPhS-C2:SD86:BTP-eC9 devices with different SVA time, measured under the illumination of AM 1.5G at 100 mW cm^{-2} .

SVA time [s]	V_{OC} [V]	J_{SC} [mA cm ⁻²]	FF [%]	PCE ^a [%]
30	0.867 (0.865 ± 0.008)	26.18 (25.90 ± 0.30)	76.99 (76.85 ± 0.20)	17.48 (17.35 ± 0.10)
	0.871 (0.865 ± 0.009)	26.56 (26.50 ± 0.15)	77.16 (76.95 ± 0.30)	18.14 (17.98 ± 0.10)
45	0.885 (0.878 ± 0.008)	26.85 (26.70 ± 0.30)	77.89 (77.75 ± 0.30)	18.51 (18.20 ± 0.25)
	0.883 (0.878 ± 0.006)	26.70 (26.65 ± 0.15)	76.79 (76.60 ± 0.25)	18.10 (17.90 ± 0.15)
75				

^aThe values in parenthesis are the average PCEs obtained from 30 devices.

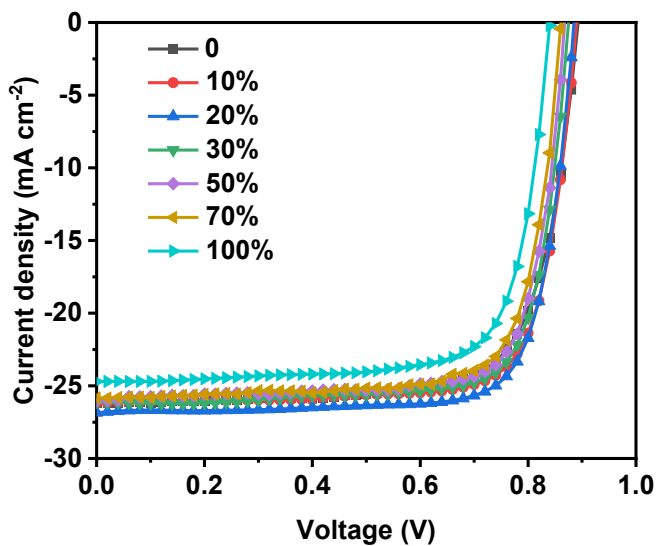


Figure S17. Relevant J - V curves of the ternary small molecule organic solar cells with different SD86 contents measured under the illumination of AM 1.5G at 100 mW cm^{-2} .

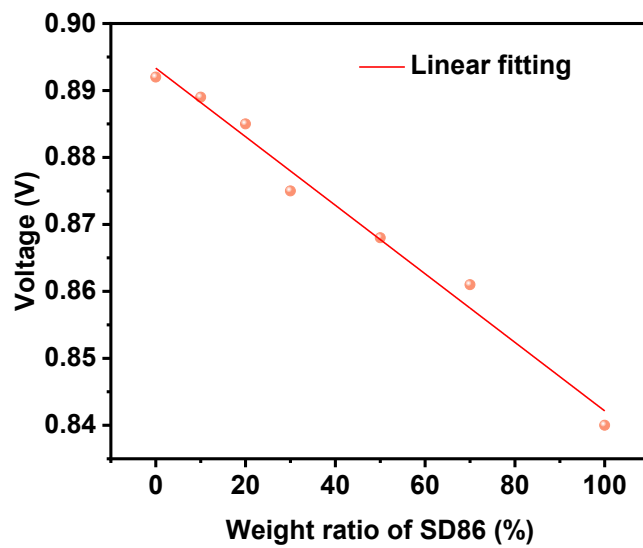


Figure S18. Composition-dependent measured V_{OC} values in the ternary devices.

Table S7. Photovoltaic parameters of the MPhS-C2:SD86:BTP-eC9 devices with different weight ratios of SD86 in the donor, measured under the illumination of AM 1.5G at 100 mW cm⁻².

Weight ratios of SD86 (%)	V_{OC} [V]	J_{SC} [mA cm ⁻²]	FF [%]	PCE ^a [%]
0	0.892 (0.888±0.006)	26.16 (25.90±0.35)	73.66 (73.50±0.30)	17.19 (17.02±0.15)
10	0.889 (0.886±0.005)	26.20 (26.10±0.25)	77.25 (77.20±0.10)	17.99 (17.85±0.10)
20	0.885 (0.878±0.008)	26.85 (26.70±0.30)	77.89 (77.75±0.30)	18.51 (18.20±0.25)
30	0.875 (0.873±0.005)	26.14 (25.90±0.35)	77.83 (77.65±0.30)	17.80 (17.60±0.15)
50	0.868 (0.865±0.004)	26.02 (25.78±0.30)	76.53 (76.40±0.20)	17.40 (17.25±0.10)
70	0.861 (0.857±0.006)	25.83 (25.72±0.25)	76.36 (76.25±0.20)	16.98 (16.80±0.15)
100	0.840 (0.836±0.005)	24.70 (24.60±0.20)	75.24 (75.05±0.25)	15.61 (15.35±0.20)

^aThe values in parenthesis are the average PCEs obtained from 30 devices.

Table S8. Summary of photovoltaic parameters with PCE > 14% in all-SMOSCs.

Active layer	V_{OC} (V)	J_{SC} (mA cm ⁻²)	FF (%)	FF× J_{SC}	PCE (%)	Ref.
BTR-Cl:Y6	0.83	23.66	74.7	17.67	14.7	[2]
BTR-Cl:Y6	0.843	24.78	74.2	18.39	15.5	[3]
BTR-Cl:N3	0.82	24.06	73.5	17.68	14.43	[4]
B1:BO-4Cl	0.83	25.27	73	18.45	15.3	[5]
B1:BTP-eC9	0.827	24.30	73.92	17.96	14.86	[6]
B1:BTP-eC9	0.832	24.98	75.44	18.84	15.68	[7]
BT-2F:N3	0.829	24.51	72.15	17.68	14.66	[8]
BT-2F:N3	0.845	24.28	75.02	18.21	15.39	[8]
SM1-F:Y6	0.866	23.25	69.9	16.25	14.07	[9]
ZR1:Y6	0.861	24.34	68.44	16.66	14.34	[10]

TBD-S4	0.854	24.53	72.10	17.69	15.10	[11]
SM-BF1:Y6	0.846	26.64	69.7	18.57	15.71	[12]
SW2:Y6	0.835	25.10	74.0	18.57	15.51	[13]
BSFTR:FO-2Cl	0.885	22.01	78.41	17.26	15.27	[14]
BSFTR:FO-EH-2Cl	0.876	22.39	80.44	18.01	15.78	[14]
Tz6T: eC9-4F	0.863	25.14	70.86	17.81	15.38	[15]
BDT-UF:N3	0.855	24.8	69.9	17.34	14.8	[16]
BDT-DF:N3	0.854	24.3	68.8	16.72	14.3	[16]
C-2F:N3	0.85	24.87	69	17.16	14.64	[17]
BM-Cl:BO-4Cl	0.826	25.90	73	18.91	15.73	[1]
BTR-Cl:BTP-FCl-FCl	0.825	24.58	75.36	18.52	15.3	[18]
L1:Y6	0.83	25.28	69.8	17.65	14.6	[19]
L2:Y6	0.83	26.35	72.1	19.00	15.8	[19]
TBFT-TR:Y6	0.784	24.59	72.78	17.90	14.03	[20]
SM-CA-Reh:N3	0.842	25.06	77.50	19.42	16.34	[21]
MPhS-C6:BTP-eC9	0.84	25.4	75.6	19.20	16.2	[22]
TB:L8-BO	0.86	24.67	74	18.26	15.8	[23]
TB-F:L8-BO	0.87	25.41	76.7	19.49	17	[23]
MPhS-C2:BTP-eC9	0.886	26.86	69.52	18.67	16.54	[24]
MPhS-C2:BTP-eC9	0.888	26.62	72.38	19.27	17.11	[24]
BO-1:BTP-eC9	0.845	25.56	77.74	19.87	16.79	[25]
HD-1:BTP-eC9	0.842	26.04	78.46	20.43	17.19	[25]
OD-1:BTP-eC9	0.828	25.49	71.89	18.32	15.18	[25]
BTR-Cl:BTP-BO-4F:Y6	0.87	24.17	68.78	16.62	14.46	[26]

BTR-Cl: Y6:PC ₇₁ BM	0.838	23.75	77.11	18.31	15.34	[27]
VC7:IT-4F: PC ₇₁ BM	0.87	23.74	73	17.33	15.08	[28]
B1:L8-BO:BO-4Cl	0.841	26.15	77.74	20.33	17.1	[29]
ZnP-TSEH:6TIC:4TIC	0.839	25.99	75.01	19.50	16.36	[30]
ZnP-TSEH:6TIC:4TIC	0.844	26.33	77.31	20.36	17.18	[30]
B1:BO-4Cl: BO-2Cl	0.84	26.05	78	20.32	17	[31]
B1:BO-4Cl:Y7	0.836	25.52	76.29	19.47	16.28	[32]
MPhS-C2:BTP-eC9:SSe-NIC	0.880	26.85	76.27	20.48	18.02	[33]
MPhS-C2:L8-BO	0.894	25.37	73.14	18.56	16.59	[34]
MPhS-C2: L8-S9	0.875	25.69	70.72	18.17	15.90	[34]
MPhS-C2:L8-BO :L8-S9	0.884	26.43	77.46	20.47	18.10	[34]
DAPor-DPP:6TIC	0.845	25.61	76.8	19.67	16.62	[35]
B2:BTP-eC9	0.861	26.2	75.8	19.86	17.1	[36]
MPhS-C2:BTP-eC9	0.892	26.16	73.66	19.27	17.19	This work
SD86:BTP-eC9	0.840	24.70	75.24	18.58	15.61	This work
MPhS-C2:SD86:BTP-eC9	0.885	26.85	77.89	20.91	18.51	This work



Figure S19. Report of certified efficiency of MPhS-C2:SD86:BTP-eC9 solar cells from National Institute of Metrology, China.

External quantum efficiency (EQE) measurements: The external quantum efficiency was measured by a Solar Cell Spectral Response Measurement System QE-R3011(Enli Technology Co., Ltd.).

Operational stability measurements: For the photostability test, the devices were fabricated without further encapsulation. We performed light-induced degradation experiments with one sun equivalent illumination intensity for 1500 hours on these photovoltaic systems investigated in this study. The devices were put inside a nitrogen-filled glovebox ($\text{H}_2\text{O} < 1 \text{ ppm}$, $\text{O}_2 < 1 \text{ ppm}$) and continuously illuminated with a white LED array (XLamp CXA1512 6500K CCT). The illumination light intensity was initially set before testing to make sure the output short-circuit current density equals the value that was measured under standard conditions mentioned earlier, and it was monitored by a photodiode (Hamamatsu S1336-8BQ) to guarantee stable light intensity. $J-V$ characters of the devices were checked periodically, and the photovoltaic parameters were calculated automatically according to the achieved $J-V$ curves. Notably, the photovoltaic parameters of devices under illumination were recorded over time and the degradation curves were shown. The cell temperature was measured occasionally, and the temperature range during aging was approximately 30 °C.

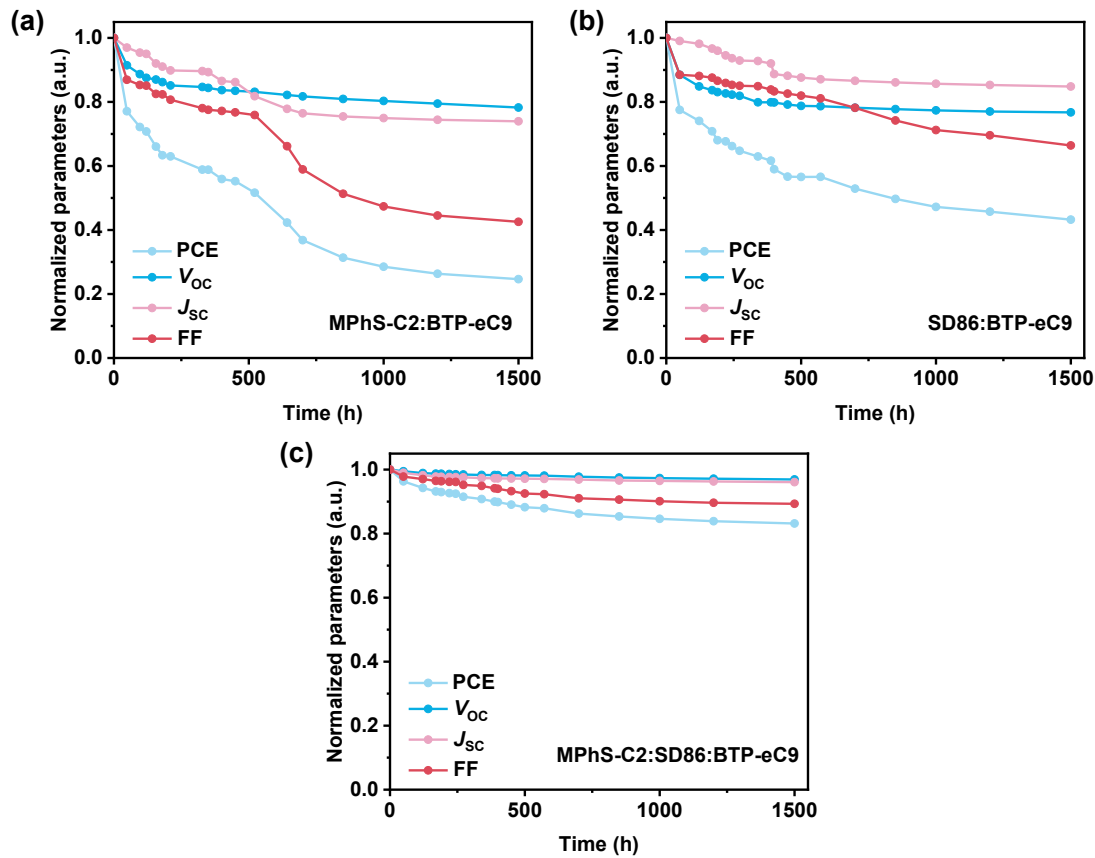


Figure S20. The normalized degradation trends of relevant photovoltaic parameters including PCE, V_{oc} , J_{sc} , and FF under continuous light-soaking for (a) MPhS-C2:BTP-eC9, (b) SD86:BTP-eC9 and (c) MPhS-C2:SD86:BTP-eC9 devices.

Table S9. The T_{80} lifetime values of all-small molecule devices reported so far.

Systems	PCE (%)	T_{80} Lifetime (h)	Ref.
MPhS-C2:BTP-eC9:SSe-NIC	18.02	436	[33]
MPhS-C2:BTP-eC9	17.16	76	[33]
MPhS-C2:SSe-NIC	16.83	62	[33]
B1:BTP-eC9	14.86	14	[6]
B1:BTP-eC9	13.92	7	[6]
BTR-F:M36	10.14	0.38	[37]
BTR-F:M36	12.19	0.66	[37]
H11:IDIC	9.73	138	[38]
BDT(TVT-SR)2:IDIC	11.10	455	[38]
DRCN5T:PC ₇₁ BM	6.73	1376	[39]
DRCN5T:PC ₇₁ BM	8.87	870	[39]
DRCN5T:PC ₇₁ BM	6.64	192	[39]
BTR:PC ₇₁ BM	9.81	78	[40]
BTR:PC ₇₁ BM	10.14	50	[40]
BTR:PC ₇₁ BM	9.16	15	[40]
BTR:PC ₇₁ BM	7.12	8	[40]
BTR:PC ₇₁ BM	6.59	65	[40]
SM-BDT:Y8	10.68	96	[41]
SM-DTBBDT:Y8	12.45	756	[41]
X2:PC ₆₁ BM	6.3	88	[42]
F3:PC ₆₁ BM	7.3	82	[42]
DRCN7T:PC ₇₁ BM	9.1	86	[42]
BTR-Cl:Y6	13.31	8	[6]
BTR-Cl:Y6	13.88	15	[6]
B1:Y6	12.32	9	[6]
B1:Y6	12.76	16	[6]
MPhS-C2:L8-BO	16.59	124	[34]
MPhS-C2: L8-S9	15.90	595	[34]
MPhS-C2:L8-BO :L8-S9	18.10	993	[34]
MPhS-C2:BTP-eC9	17.19	45	This work
SD86:BTP-eC9	15.61	45	This work
MPhS-C2:SD86:BTP-eC9	18.51	3100	This work

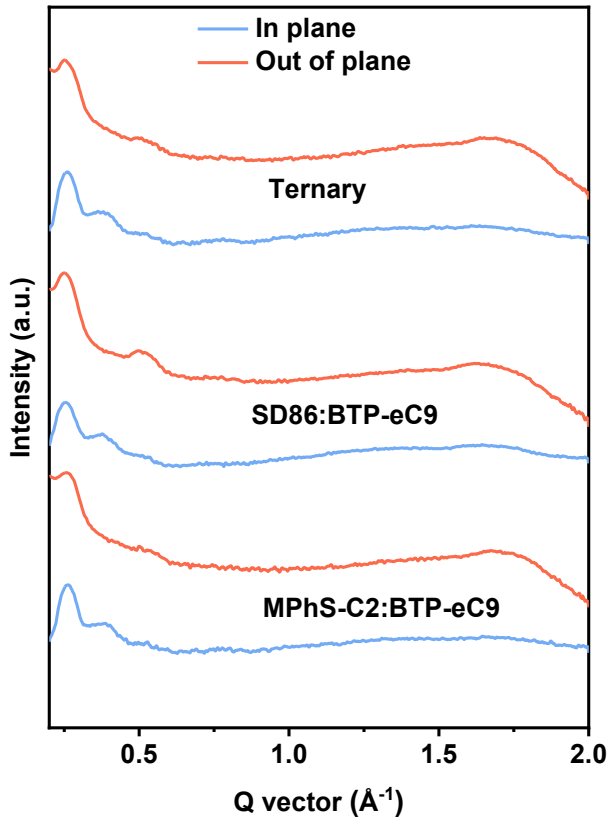


Figure S21. Scattering profiles of in-plane and out-of-plane for the binary and ternary blend films.

Table S10. Summarized parameters for the ordering structures of the blend films.

Materials	In-plane (100)			Out-of-plane (010)		
	q (\AA^{-1})	d -spacing (\AA)	q (\AA^{-1})	d -spacing (\AA)	FWHM (\AA^{-1})	L_c (\AA)
MPhS-C2:BTP-eC9	0.26	24.15	1.67	3.76	0.206	30.49
SD86:BTP-eC9	0.26	24.15	1.67	3.76	0.183	34.32
MPhS-C2:SD86:BTP-eC9	0.26	24.15	1.69	3.72	0.147	42.72

Atomic force microscopy (AFM) measurements: AFM measurements were performed by using a Nano Wizard 4 atomic force microscopy (JPK Inc. Germany) in Qi mode to observe the film surface morphologies of the ITO/PEDOT:PSS/active layer.

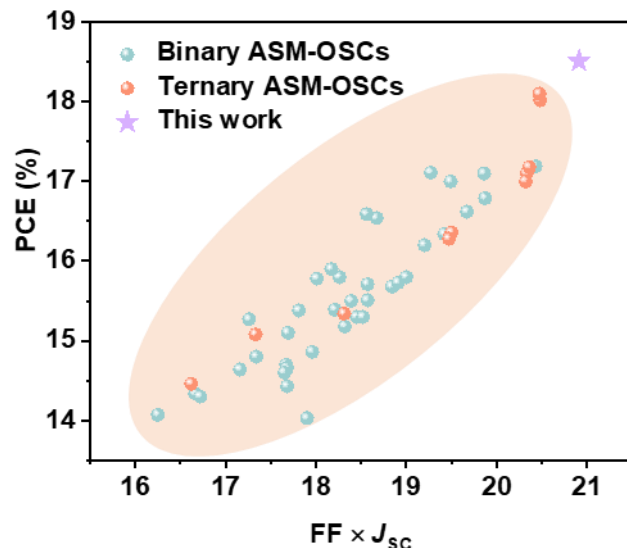


Figure S22. Plots of the PCE versus $\text{FF} \times J_{\text{SC}}$ for the efficient binary and ternary all-SMOSCs reported in the literature. Our results illustrate that active layer morphology modulated by materials design and donor-alloy strategy pushed the development of all-SMOSCs.

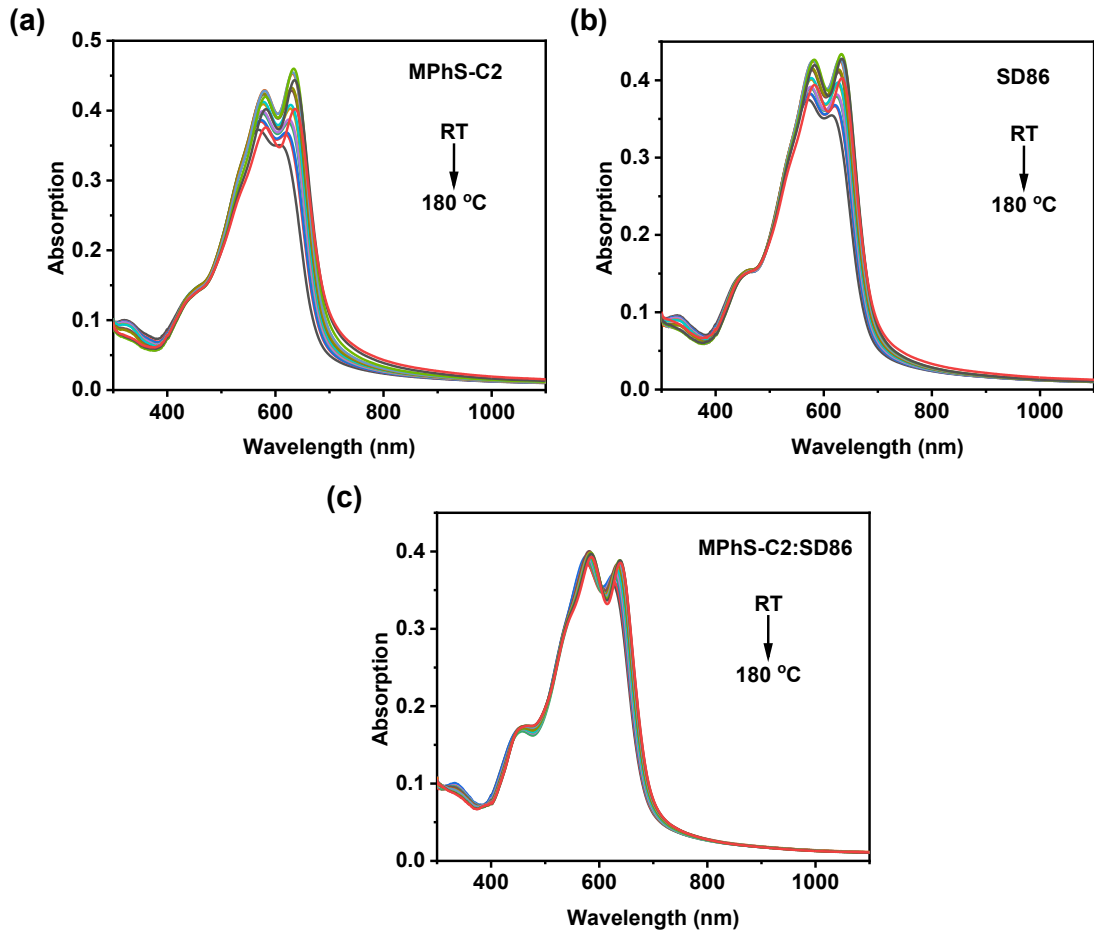


Figure S23. *UV-vis-NIR* absorption spectra of (a) MPhS-C2, (b) SD86, and (c) MPhS-C2:SD86 with the increasing thermal annealing temperature. Evolution of the deviation Metric (DM_T) as a function of annealing temperature, illustrating a phase transition of (a) MPhS-C2 (105.9 ± 1 °C), (b) SD86 (108.3 ± 1 °C) and (c) MPhS-C2:SD86 (133.5 ± 1 °C). Notably, the DM_T factor represents the sum of squared deviations in absorbance between un-annealed and annealed films: $DM_T = \sum_{\lambda_{\min}}^{\lambda_{\max}} [(I_{RT}(\lambda) - I_T(\lambda))^2]$, where λ , λ_{\min} , and λ_{\max} are explained as the wavelength, the lower and upper bounds of the optical sweep, $I_{RT}(\lambda)$ and $I_T(\lambda)$ are explained as the normalized absorption intensities of un-annealed and annealed films, respectively. When the overall absorption intensity changes significantly, it suggests that the inherent properties of the material have undergone a glass transition, and the corresponding temperature is phase transition temperature (T_{pt}).

Transient absorption spectroscopy (TAS): For femtosecond transient absorption spectroscopy, the fundamental output from Yb:KGW laser (1030 nm, 220 fs Gaussian fit, 100 kHz, Light Conversion Ltd) was separated into two light beams. One was introduced to NOPA (ORPHEUS-N, Light Conversion Ltd) to produce a certain wavelength for the pump beam (here we use 780 nm), and the other was focused onto a YAG plate to generate a white light continuum as a probe beam. The pump and probe overlapped on the sample at a small angle of less than 10°. The transmitted probe light from the sample was collected by a linear CCD array. Then we obtained transient differential, transmission signals by the equation shown below:

$$\frac{\Delta T}{T} = \frac{T_{\text{pump-on}} - T_{\text{pump-off}}}{T_{\text{pump-off}}}$$

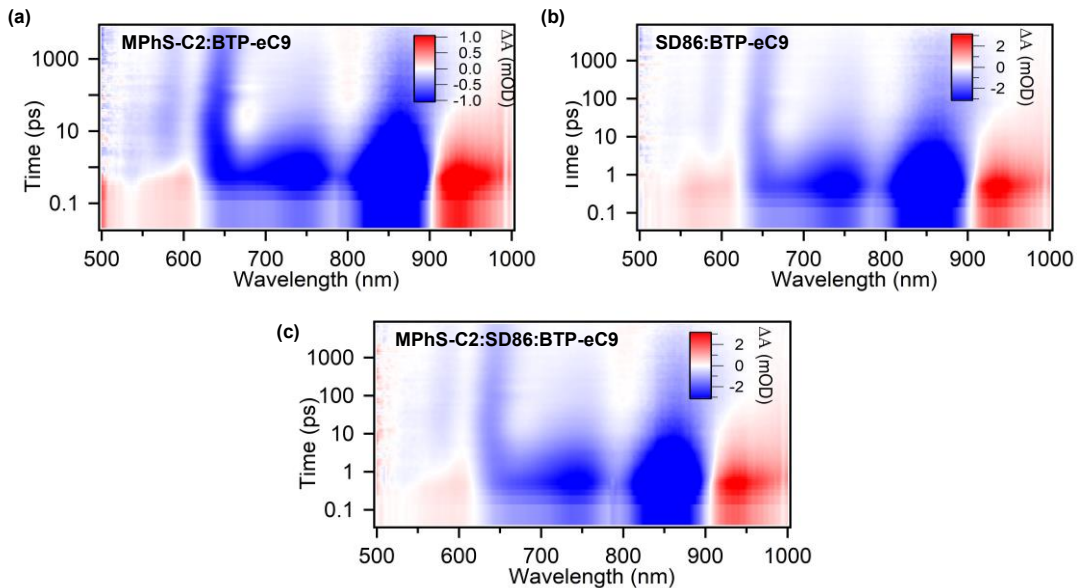


Figure S24. The TA images of (A) MPhS-C2:BTP-eC9 film, (B) SD86:BTP-eC9 film, and (C) MPhS-C2:SD86:BTP-eC9 film under 780 nm pump with a power flux of 48 $\mu\text{J cm}^{-2}$.

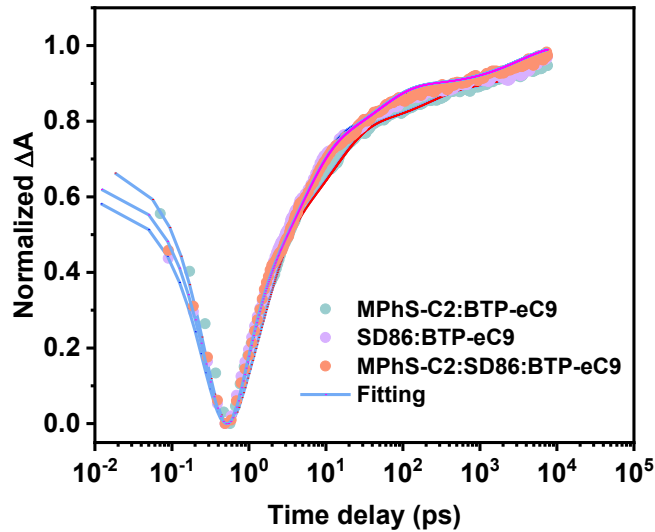


Figure S25. Comparison of the hole transfer kinetics for the binary and ternary blends.

Table S11. Parameters constants of A1, τ_1 , and A2 τ_2 of different blends.

Systems	A1	τ_1 (ps)	A2	τ_2 (ps)	Average τ_h (ps)
MPhS-C2:BTP-eC9	69.1%	1.20	30.9%	12.17	4.59
SD86:BTP-eC9	62.4%	0.69	37.6%	4.85	2.25
MPhS-C2:SD86:BTP-eC9	62.7%	0.56	37.3%	4.51	2.03

FTPS-EQE spectra measurements: The FTPS measurements were recorded using a Bruker Vertex 70 Fourier-transform infrared (FTIR) spectrometer, equipped with a quartz tungsten halogen lamp, a quartz beam-splitter, and an external detector option. A low noise current amplifier (Femto DLPCA-200) was used to amplify the photocurrent produced on the illumination of the photovoltaic devices with light modulated by the FTIR. The output voltage of the current amplifier was fed back into the external detector port of the FTIR. The photocurrent spectrum was collected by FTIR's software.

Urbach energy measurement: The energetic disorder can be quantized by a parameter of Urbach energy (E_U), which follows the Urbach rule expressed as follows:

$$\alpha(E) = \alpha_0 e^{\frac{(E-E_0)}{E_U}}$$

Wherein, $\alpha(E)$ is the absorption coefficient, α_0 and E_0 are two constants, and E is the photon energy. The smaller E_U represents the lower energetic disorder. By fitting the FTPS-EQE curves with the above Equation, the E_U values can be obtained.

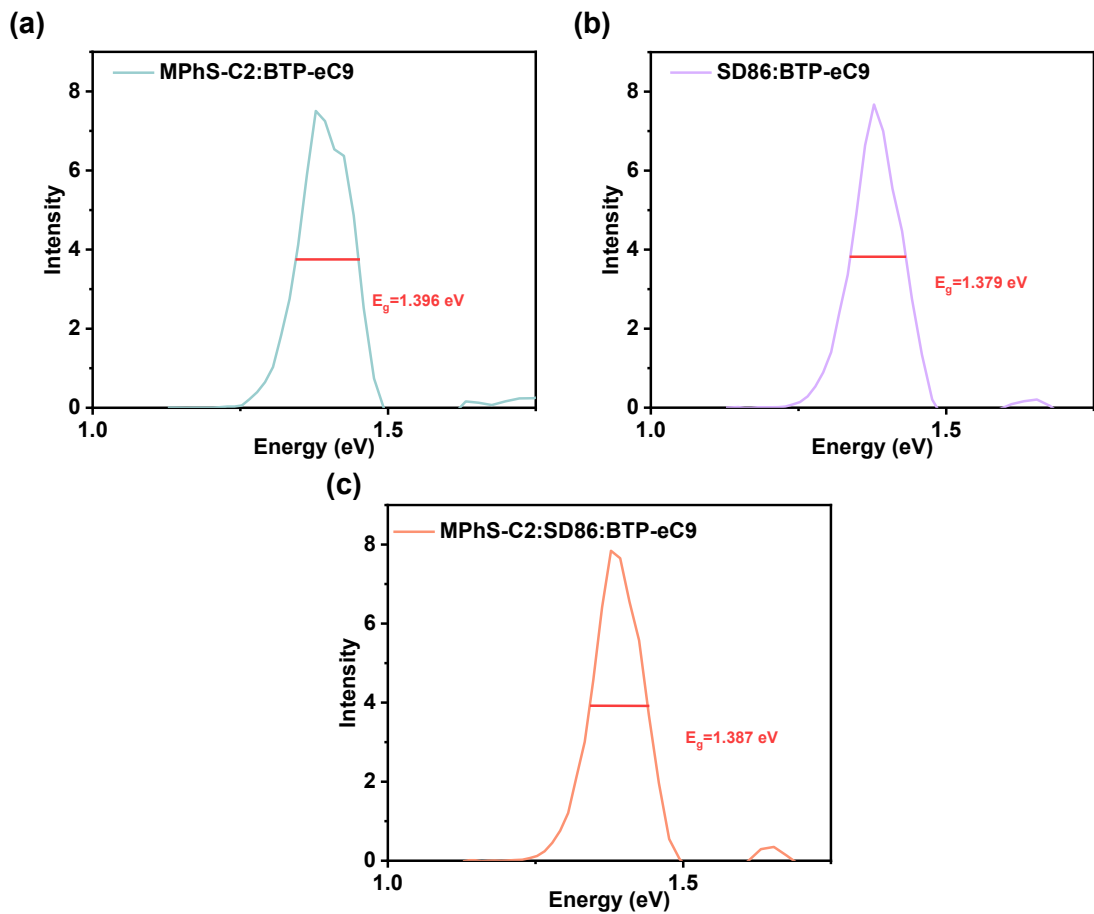


Figure S26. Bandgap distributions for all-SMOSCs based on (a) MPhS-C2:BTP-eC9, (b) SD86:BTP-eC9, and (c) MPhS-C2:SD86:BTP-eC9 blends. The E_g value is determined by the derivatives of the FTPS-EQE curve and then calculated according to the literature.

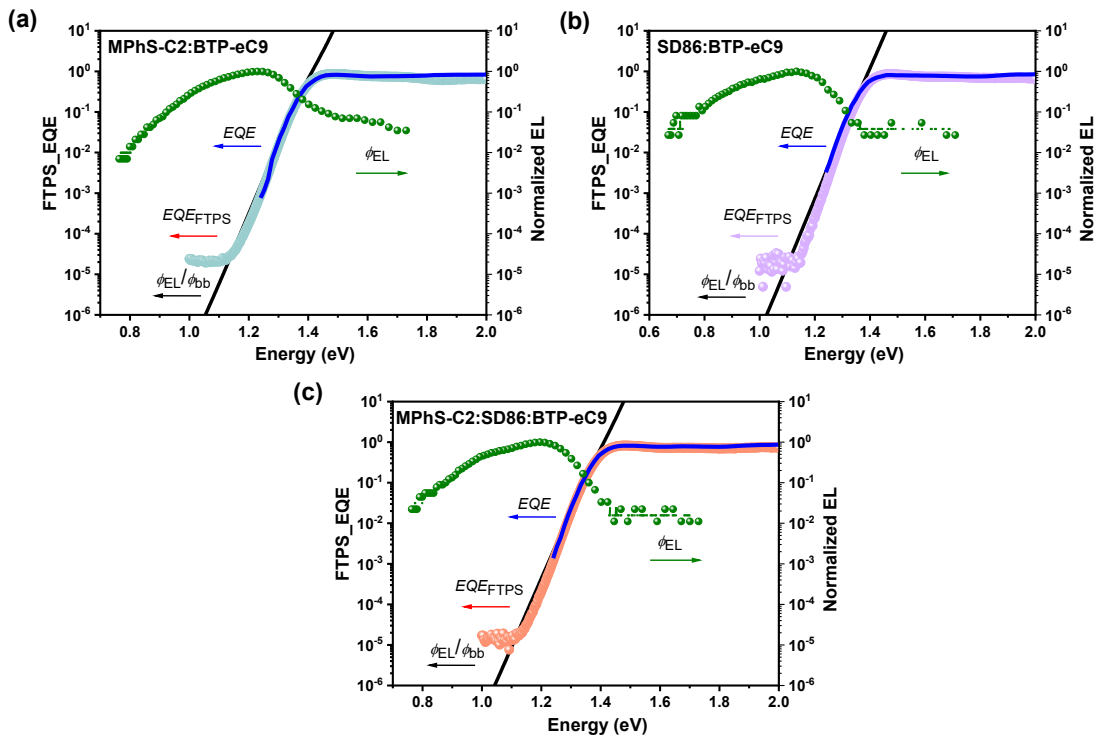


Figure S27. Semilogarithmic plots of normalized EL spectra, measured EQE spectra, and FTPS-EQE spectra as a function of energy for devices based on (a) MPhS-C2:BTP-eC9, (b) SD86:BTP-eC9, and (c) MPhS-C2:SD86:BTP-eC9 blends.

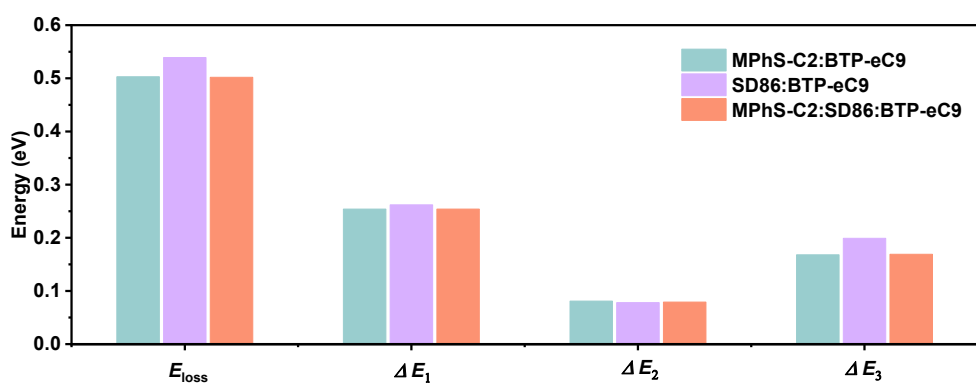


Figure S28. Diagram of different parts of energy losses in three systems.

Table S12. Measured and calculated parameters to quantify the non-radiative recombination losses of the binary and ternary devices.

Systems	E_g^a (eV)	V_{oc}^b (V)	E_{loss} (eV)	V_{oc}^{SQ} (V)	ΔE_1 (eV)	$V_{oc}^{rad\ c}$ (V)	ΔE_2 (eV)	ΔE_3 (eV)
MPhS-C2:BTP-eC9	1.396	0.892	0.504	1.142	0.254	1.061	0.081	0.169
SD86:BTP-eC9	1.379	0.840	0.539	1.117	0.262	1.038	0.078	0.199
MPhS-C2:SD86:BTP-eC9	1.387	0.885	0.502	1.133	0.254	1.054	0.079	0.169

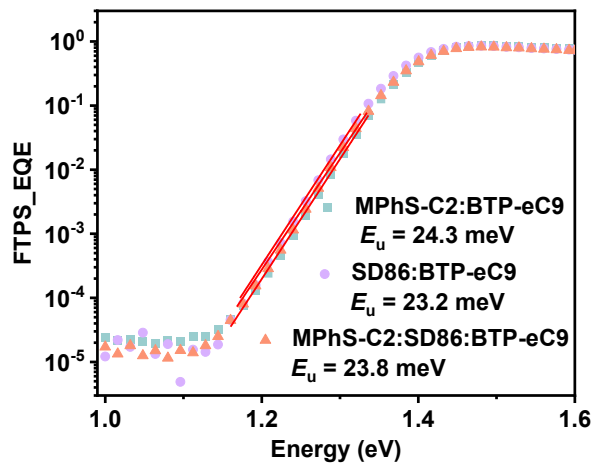


Figure S29. FTPS-EQE of the binary and ternary devices at the absorption onset.

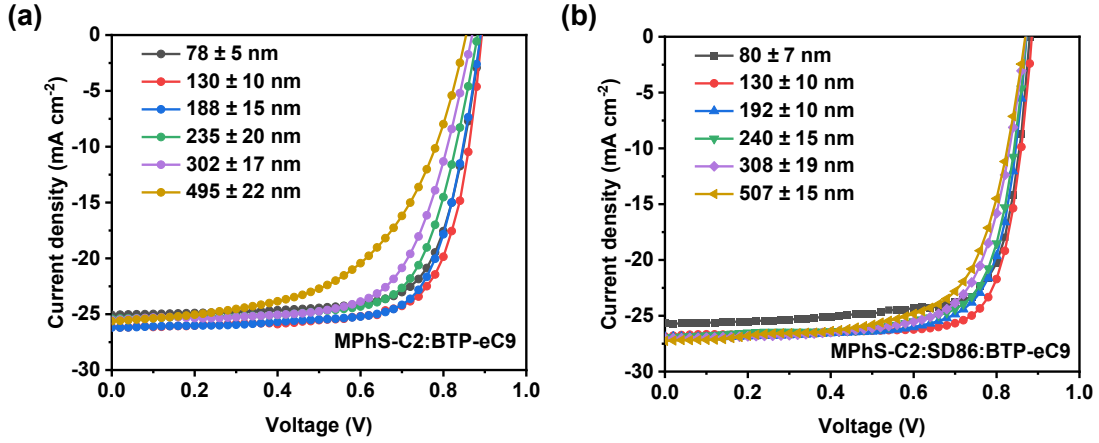


Figure S30. J - V characteristics for devices based on (a) MPhS-C2:BTP-eC9 and (b) MPhS-C2:SD86:BTP-eC9, with different active layer thicknesses, measured under the illumination of AM 1.5 G at 100 mW cm^{-2} .

Table S13. Summary of photovoltaic parameters of the all-SMOSCs based on MPhS-C2:BTP-eC9 and MPhS-C2:SD86:BTP-eC9 with different active layer thickness, measured under the illumination of AM 1.5 G at 100 mW cm^{-2} .

Systems	Thickness (nm)	V_{OC} (V)	J_{SC} (mA/cm^2)	FF (%)	PCE ^a (%)
MPhS-C2: BTP-eC9	78±5	0.891 (0.890±0.005)	25.06 (24.90±0.20)	72.71 (72.60±0.15)	16.24 (16.10±0.10)
	130±10	0.892 (0.888±0.006)	26.16 (25.90±0.35)	73.66 (73.50±0.30)	17.19 (17.02±0.15)
	188±15	0.890 (0.885±0.007)	26.20 (26.15±0.15)	72.95 (72.85±0.15)	17.01 (16.80±0.20)
	235±20	0.883 (0.880±0.005)	25.41 (25.30±0.20)	70.71 (70.65±0.10)	15.87 (15.70±0.15)
	302±17	0.869 (0.865±0.005)	25.52 (25.25±0.35)	67.22 (67.10±0.15)	14.91 (14.50±0.35)
	495±22	0.855 (0.850±0.008)	25.63 (25.50±0.30)	55.96 (55.75±0.30)	12.26 (12.00±0.25)
MPhS-C2:SD86: BTP-eC9	80±7	0.880 (0.875±0.007)	25.69 (25.50±0.25)	76.20 (76.10±0.15)	17.23 (17.10±0.10)
	130±10	0.885 (0.878±0.008)	26.85 (26.70±0.30)	77.89 (77.75±0.30)	18.51 (18.20±0.25)
	192±10	0.872 (0.869±0.005)	26.90 (26.85±0.30)	75.11 (75.00±0.25)	17.62 (17.40±0.15)
	240±15	0.872 (0.867±0.006)	26.94 (26.88±0.20)	73.43 (73.15±0.35)	17.25 (17.00±0.20)
	308±19	0.870 (0.865±0.008)	27.02 (26.95±0.30)	70.98 (70.80±0.30)	16.69 (16.40±0.20)
	507±15	0.869 (0.863±0.007)	27.25 (27.10±0.25)	67.40 (67.25±0.20)	15.96 (15.60±0.30)

^aThe values in parenthesis are the average PCEs obtained from 30 devices.

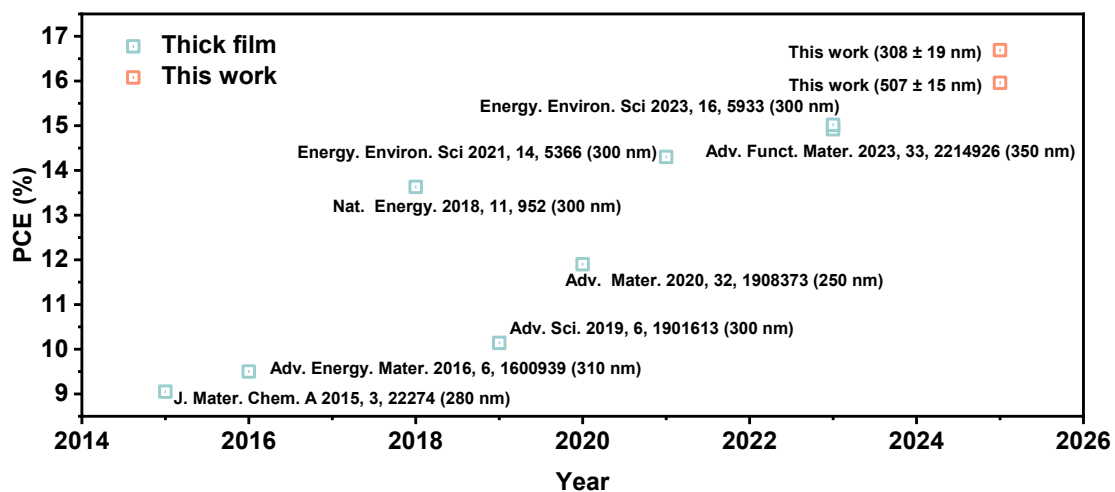


Figure S31. Summary of the highest PCEs of thick-film all-SMOSCs reported in the recent years.

Table S14. The reported PCEs of relevant binary and ternary all-SMOSC devices based on thick active layers, measured under one-sun illumination.

Active layer	Thickness (nm)	V _{OC} (V)	J _{SC} (mA cm ⁻²)	FF (%)	PCE (%)	Ref.
DR3TSBDT:PC ₇₁ BM	280	0.88	15.82	65.3	9.05	[43]
BTR:PC ₇₁ BM	310	0.94	14.5	70	9.5	[44]
BTR:NITI:PC ₇₁ BM	300	0.94	19.5	73.83	13.63	[45]
BTR:BTR-OH:PC ₇₁ BM	300	0.93	14.62	74.2	10.14	[46]
SM1-F:Y6	250	0.85	21.9	64	11.9	[9]
L2:Y6	300	0.82	24.5	71.2	14.3	[19]
HD-1:BTP-eC9	350	0.811	27.25	67.52	14.92	[25]
T27:Y6	300	0.812	27.21	68.02	15.03	[47]
MPhS-C2:SD86:BTP-eC9	308±19	0.870	27.02	70.98	16.69	This work
MPhS-C2:SD86:BTP-eC9	507±15	0.869	27.25	67.40	15.96	This work

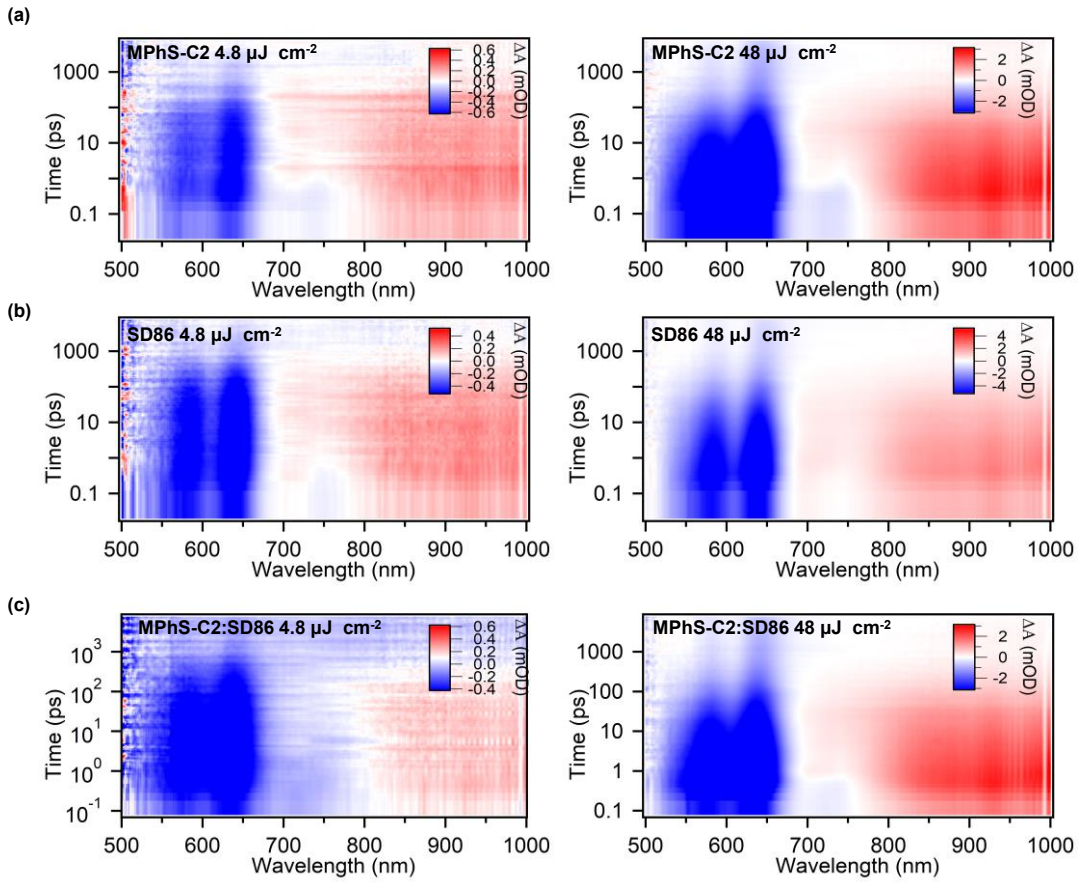


Figure S32. The TA images of (a) MPhS-C2 neat film, (b) SD86 neat film, and (c) MPhS-C2: SD86 film under 550 nm pump with a power flux of 4.8 and 48 $\mu\text{J cm}^{-2}$.

Table S15. Detailed parameters of single exciton decay dynamic for neat and the alloy donor films.

Films	Pump energy [$\mu\text{J cm}^{-2}$]	t [ps]	k_1 [$\times 10^{10} \text{ ps}^{-1}$]	k_2 [$\times 10^{10} \text{ ps}^{-1}$]	D [$\times 10^{-3} \text{ cm}^2 \text{ s}^{-1}$]	L_D [nm]
MPhS-C2	4.8	251.5	0.39	/	/	/
	48	/	/	1.88	7.48	13.7
SD86	4.8	351.8	0.28	/	/	/
	48	/	/	3.86	15.36	23.3
MPhS-C2:SD86	4.8	321.6	0.31	/	/	/
	48	/	/	5.38	21.41	26.3

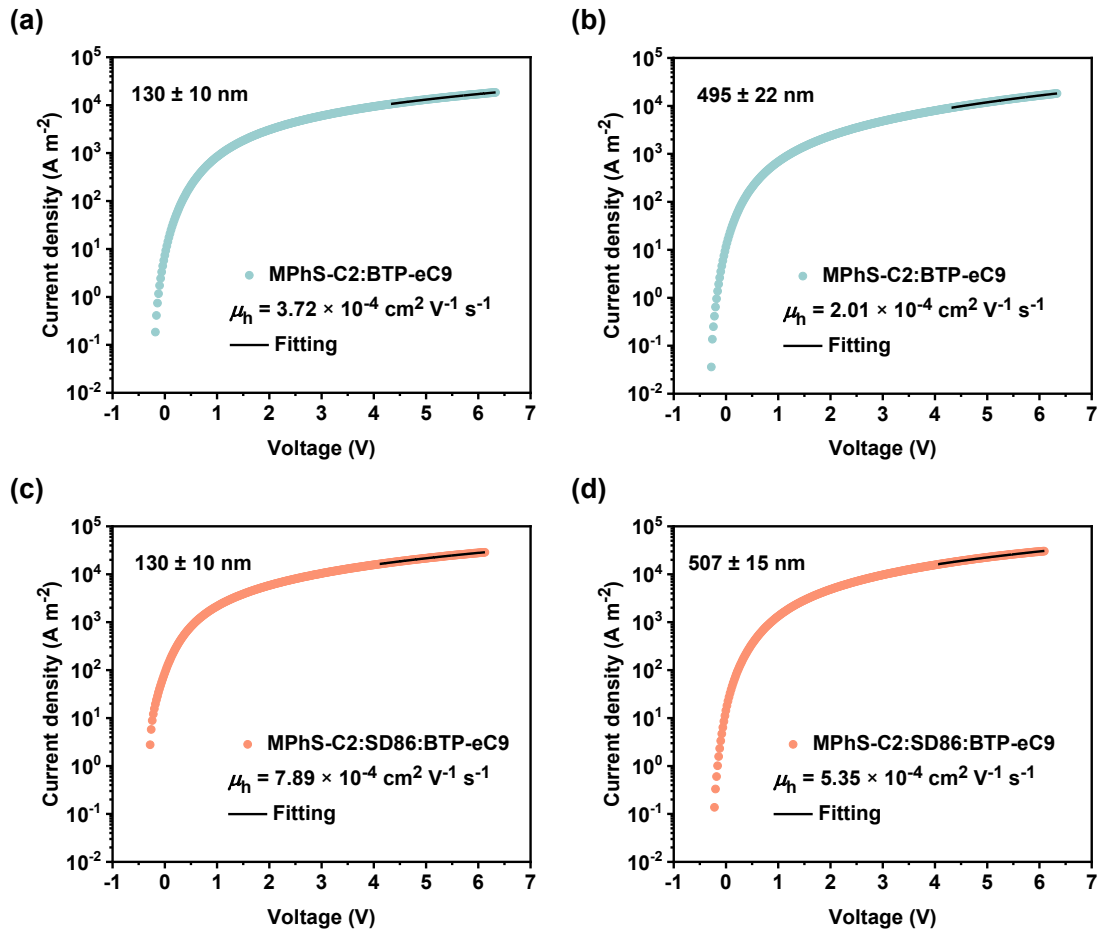


Figure S33. The hole-only mobilities of the binary devices based on the (a) thin blend and (b) thick blend, and the ternary devices based on the (c) thin blend and (d) thick blend, measured using the space-charge-limited-current approach.

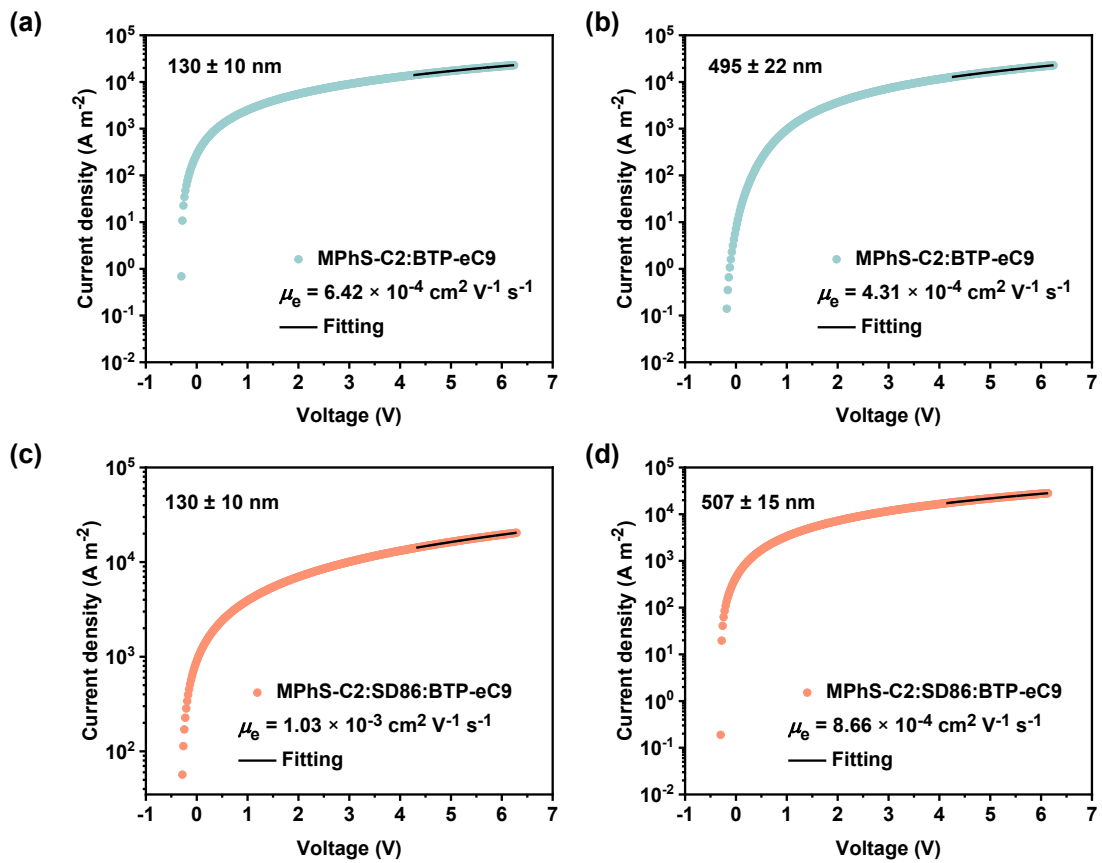


Figure S34. The electron-only mobilities of the binary devices based on the (a) thin blend and (b) thick blend, and the ternary devices based on the (c) thin blend and (d) thick blend, measured using the space-charge-limited-current approach.

Transient photovoltage (TPV) measurements: In the TPV measurements, a 405 nm laser diode was used to keep the organic solar cells in the V_{OC} conditions. Measuring the light intensity with a highly linear photodiode and driving the laser intensity with a waveform generator (Agilent 33500B) allowed reproducible adjustments of the light intensities under one sun. Moreover, a small perturbation was induced with a second 405 nm laser diode. The intensity of the short laser pulse was adjusted to keep the voltage perturbation below 10 mV. After the pulse, the voltage decays back to its steady state value in a single exponential decay.

Table S16. Summary of photovoltaic parameters of the corresponding binary and ternary devices with different active layer thickness (≈ 130 nm, ≈ 500 nm), measured under the illumination of AM 1.5 G at 100 mW cm^{-2} .

Systems	Thickness (nm)	V_{OC} (V)	J_{SC} (mA/cm ²)	FF (%)	PCE ^{a)} (%)
MPhS-C2:Y6	128 ± 6	0.855 (0.850 \pm 0.08)	25.01 (24.90 \pm 0.20)	74.24 (74.15 \pm 0.15)	15.88 (15.70 \pm 0.10)
	503 ± 18	0.803 (0.795 \pm 0.10)	23.97 (23.85 \pm 0.20)	55.32 (55.05 \pm 0.30)	10.65 (10.45 \pm 0.15)
MPhS-C2: SD86:Y6	130 ± 8	0.853 (0.845 \pm 0.09)	25.52 (25.45 \pm 0.15)	75.06 (74.95 \pm 0.20)	16.34 (16.15 \pm 0.15)
	505 ± 15	0.847 (0.845 \pm 0.05)	26.15 (25.90 \pm 0.30)	65.43 (65.10 \pm 0.40)	14.49 (14.30 \pm 0.15)
MPhS-C2:N3	126 ± 6	0.831 (0.825 \pm 0.07)	25.54 (25.50 \pm 0.10)	75.38 (75.25 \pm 0.15)	16.00 (15.70 \pm 0.25)
	510 ± 20	0.799 (0.795 \pm 0.06)	24.65 (24.40 \pm 0.30)	55.18 (55.00 \pm 0.30)	10.87 (10.55 \pm 0.25)
MPhS-C2: SD86:N3	132 ± 5	0.835 (0.830 \pm 0.08)	25.98 (25.90 \pm 0.15)	77.33 (77.15 \pm 0.20)	16.78 (16.60 \pm 0.15)
	508 ± 15	0.831 (0.825 \pm 0.08)	26.32 (26.15 \pm 0.25)	69.00 (68.75 \pm 0.35)	15.09 (14.80 \pm 0.25)
MPhS-C2:L8-BO	135 ± 12	0.902 (0.900 \pm 0.05)	25.28 (25.20 \pm 0.20)	73.63 (73.55 \pm 0.15)	16.79 (16.65 \pm 0.10)
	496 ± 10	0.862 (0.855 \pm 0.10)	24.30 (24.05 \pm 0.35)	58.07 (57.85 \pm 0.30)	12.16 (11.80 \pm 0.30)
MPhS-C2: SD86:L8-BO	137 ± 8	0.890 (0.885 \pm 0.07)	26.51 (26.40 \pm 0.20)	76.13 (76.05 \pm 0.10)	17.96 (17.70 \pm 0.20)
	502 ± 16	0.883 (0.875 \pm 0.10)	26.75 (26.60 \pm 0.30)	66.74 (66.55 \pm 0.25)	15.76 (15.50 \pm 0.25)

^aThe values in parenthesis are the average PCEs obtained from 10 devices.

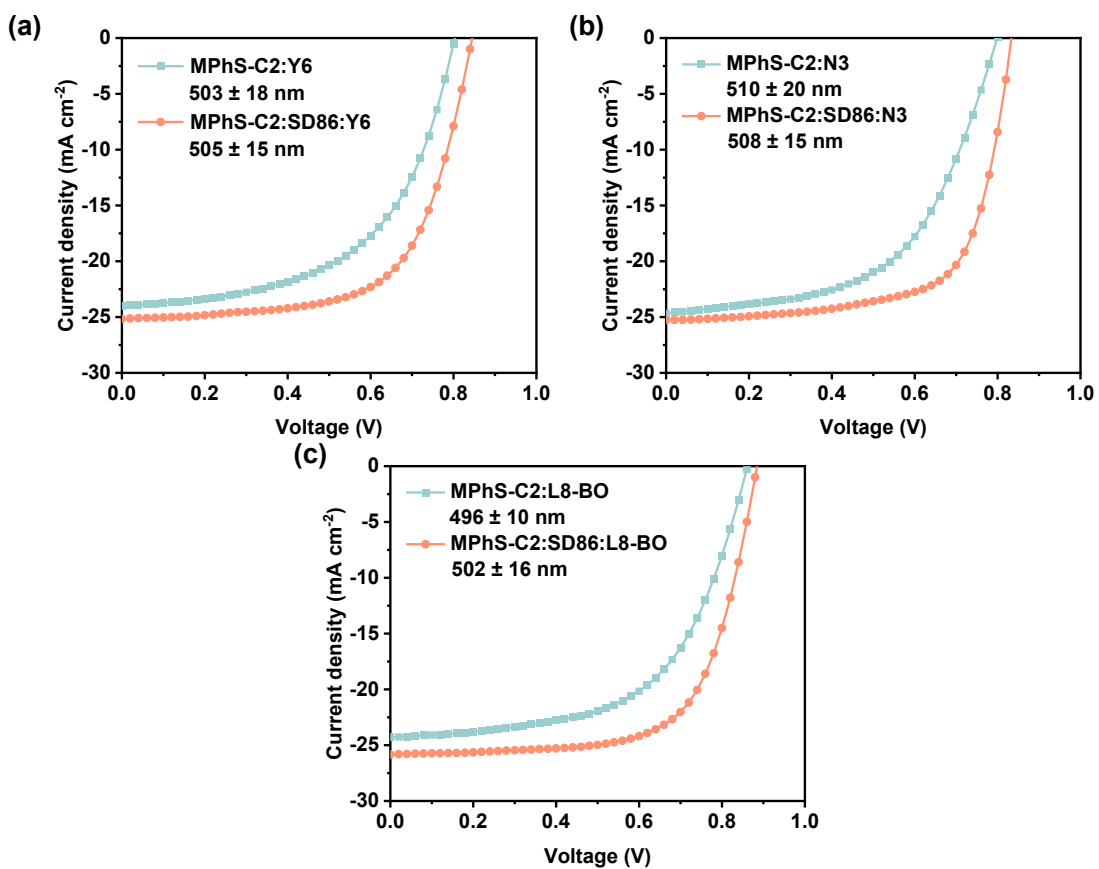


Figure S35. J - V characteristics of the corresponding binary and ternary devices based on (a) Y6, (b) N3, and (c) L8-BO as the acceptor, with the active layer thickness (\approx 500 nm).

Reference

- W. Gao, M. Jiang, Z. Wu, B. Fan, W. Jiang, N. Cai, H. Xie, F. R. Lin, J. Luo, Q. An, H. Y. Woo and A. K. Y. Jen, *Angew. Chem. Int. Ed.*, 2022, **61**, 202205168
- H. Tang, H. Chen, C. Yan, J. Huang, P. W. K. Fong, J. Lv, D. Hu, R. Singh, M. Kumar, Z. Xiao, Z. Kan, S. Lu and G. Li, *Adv. Energy Mater.*, 2020, **10**, 2001076.
- D. Hu, Q. Chen, J. Zhang and S. Lu, *Sustainable Energy Fuels*, 2022, **6**, 5256-5260.
- S. Chen, J. Ye, Q. Yang, J. Oh, D. Hu, K. Yang, G. O. Odunmbaku, F. Li, Q. Yu, Z. Kan, Z. Xiao, C. Yang, S. Lu and K. Sun, *J. Mater. Chem. A*, 2021, **9**, 2857-2863.
- J. Qin, C. An, J. Zhang, K. Ma, Y. Yang, T. Zhang, S. Li, K. Xian, Y. Cui, Y. Tang, W. Ma, H. Yao, S. Zhang, B. Xu, C. He and J. Hou, *Sci China Mater*, 2020, **63**, 1142-1150.
- R. Sun, Y. Wu, J. Guo, Y. Wang, F. Qin, B. Shen, D. Li, T. Wang, Y. Li, Y. Zhou, G. Lu, Y. Li and J. Min, *Energy Environ. Sci.*, 2021, **14**, 3174-3183.

7. M. Jiang, H.-R. Bai, H.-F. Zhi, J.-K. Sun, J.-L. Wang, F. Zhang and Q. An, *ACS Energy Lett.*, 2021, **6**, 2898-2906.
8. J. Ge, L. Hong, W. Song, L. Xie, J. Zhang, Z. Chen, K. Yu, R. Peng, X. Zhang and Z. Ge, *Adv. Energy Mater.*, 2021, **11**, 2100800.
9. B. Qiu, Z. Chen, S. Qin, J. Yao, W. Huang, L. Meng, H. Zhu, Y. Yang, Z. G. Zhang and Y. Li, *Adv. Mater.*, 2020, **32**, 1908373.
10. R. Zhou, Z. Jiang, C. Yang, J. Yu, J. Feng, M. A. Adil, D. Deng, W. Zou, J. Zhang, K. Lu, W. Ma, F. Gao and Z. Wei, *Nat. Commun.*, 2019, **10**, 5393.
11. X. Wang, J. Wang, J. Han, D. Huang, P. Wang, L. Zhou, C. Yang, X. Bao and R. Yang, *Nano Energy*, 2021, **81**, 105612.
12. J. Guo, B. Qiu, D. Yang, C. Zhu, L. Zhou, C. Su, U. S. Jeng, X. Xia, X. Lu, L. Meng, Z. Zhang and Y. Li, *Adv. Funct. Mater.*, 2021, **32**, 2110159.
13. S. Wu, W. Feng, L. Meng, Z. Zhang, X. Si, Y. Chen, X. Wan, C. Li, Z. Yao and Y. Chen, *Nano Energy*, 2022, **103**, 107801.
14. L. Meng, M. Li, G. Lu, Z. Shen, S. Wu, H. Liang, Z. Li, G. Lu, Z. Yao, C. Li, X. Wan and Y. Chen, *Small*, 2022, **18**, 2201400.
15. T. Duan, Q. Chen, Q. Yang, D. Hu, G. Cai, X. Lu, J. Lv, H. Song, C. Zhong, F. Liu, D. Yu and S. Lu, *J. Mater. Chem. A*, 2022, **10**, 3009-3017.
16. Q. Ye, J. Ge, D. Li, Z. Chen, J. Shi, X. Zhang, E. Zhou, D. Yang and Z. Ge, *ACS Appl. Mater. Interfaces*, 2022, **14**, 33234-33241.
17. S. Cai, P. Huang, G. Cai, X. Lu, D. Hu, C. Hu and S. Lu, *ACS Appl. Mater. Interfaces*, 2022, **14**, 14532-14540.
18. D. Hu, Q. Yang, Y. Zheng, H. Tang, S. Chung, R. Singh, J. Lv, J. Fu, Z. Kan, B. Qin, Q. Chen, Z. Liao, H. Chen, Z. Xiao, K. Sun and S. Lu, *Adv. Sci.* , 2021, **8**, 2004262.
19. T. Xu, J. Lv, K. Yang, Y. He, Q. Yang, H. Chen, Q. Chen, Z. Liao, Z. Kan, T. Duan, K. Sun, J. Ouyang and S. Lu, *Energy Environ. Sci.*, 2021, **14**, 5366-5376.
20. R. Sun, Y. Wu, J. Guo, Z. Luo, C. Yang and J. Min, *Sci China Chem*, 2020, **63**, 1246-1255.
21. J. Ge, L. Hong, H. Ma, Q. Ye, Y. Chen, L. Xie, W. Song, D. Li, Z. Chen, K. Yu, J. Zhang, Z. Wei, F. Huang and Z. Ge, *Adv. Mater.*, 2022, **34**, 2202752.
22. L. Zhang, X. Zhu, D. Deng, Z. Wang, Z. Zhang, Y. Li, J. Zhang, K. Lv, L. Liu, X. Zhang, H. Zhou, H. Ade and Z. Wei, *Adv. Mater.*, 2021, **34**, 2106316.
23. Z. Li, X. Wang, N. Zheng, A. Saparbaev, J. Zhang, C. Xiao, S. Lei, X. Zheng, M. Zhang, Y. Li, B. Xiao and R. Yang, *Energy Environ. Sci.*, 2022, **15**, 4338-4348.
24. L. Zhang, R. Sun, Z. Zhang, J. Zhang, Q. Zhu, W. Ma, J. Min, Z. Wei and D. Deng, *Adv. Mater.*, 2022, **34**, 2207020.
25. K. Ma, W. Feng, H. Liang, H. Chen, Y. Wang, X. Wan, Z. Yao, C. Li, B. Kan and Y. Chen, *Adv. Funct. Mater.*, 2023, **33**, 2214926.
26. C. Xu, H. Chen, Z. Zhao, J. Gao, X. Ma, S. Lu, X. Zhang, Z. Xiao and F. Zhang, *J. Energy Chem.*, 2021, **57**, 610-617.
27. D. Hu, Q. Yang, H. Chen, F. Wobben, V. M. Le Corre, R. Singh, T. Liu, R. Ma, H. Tang, L. J. A. Koster, T. Duan, H. Yan, Z. Kan, Z. Xiao and S. Lu, *Energy*

- Environ. Sci.*, 2020, **13**, 2134-2141.
28. H. Dahiya, V. Cuesta, P. de la Cruz, F. Langa and G. D. Sharma, *ACS Appl. Energy Mater.*, 2021, **4**, 4498-4506.
29. M. Jiang, H.-F. Zhi, B. Zhang, C. Yang, A. Mahmood, M. Zhang, H. Y. Woo, F. Zhang, J.-L. Wang and Q. An, *ACS Energy Lett.*, 2023, **8**, 1058-1067.
30. Y. Sun, L. Nian, Y. Kan, Y. Ren, Z. Chen, L. Zhu, M. Zhang, H. Yin, H. Xu, J. Li, X. Hao, F. Liu, K. Gao and Y. Li, *Joule*, 2022, **6**, 2835-2848.
31. J. Qin, Z. Chen, P. Bi, Y. Yang, J. Zhang, Z. Huang, Z. Wei, C. An, H. Yao, X. Hao, T. Zhang, Y. Cui, L. Hong, C. Liu, Y. Zu, C. He and J. Hou, *Energy Environ. Sci.*, 2021, **14**, 5903-5910.
32. M. Jiang, H. Bai, H. Zhi, L. Yan, H. Y. Woo, L. Tong, J. Wang, F. Zhang and Q. An, *Energy Environ. Sci.*, 2021, **14**, 3945-3953.
33. Y. Gao, X. Yang, W. Wang, R. Sun, J. Cui, Y. Fu, K. Li, M. Zhang, C. Liu, H. Zhu, X. Lu and J. Min, *Adv. Mater.*, 2023, **35**, 2300531.
34. Y. Gao, X. Yang, R. Sun, L.-Y. Xu, Z. Chen, M. Zhang, H. Zhu and J. Min, *Joule*, 2023, **7**, 2845-2858.
35. W. Zou, X. Zhang, H. Shen, W. Zhang, X. Jiang, L. Ni, C. Shen, L. Geng, X. Hao, Y. Yang, X. Wang, R. Yang, Y. Sun, Y. Kan and K. Gao, *SusMat.*, 2024, **4**, e203.
36. T. Zhang, C. An, P. Bi, K. Xian, Z. Chen, J. Wang, Y. Xu, J. Dai, L. Ma, G. Wang, X. Hao, L. Ye, S. Zhang and J. Hou, *Energy Environ. Sci.*, 2024, **17**, 3927-3936.
37. P. Yin, Y. Ma and Q. Zheng, *J. Mater. Chem. A*, 2022, **10**, 10400-10407.
38. J. Guo, H. Bin, W. Wang, B. Chen, J. Guo, R. Sun, Z.-G. Zhang, X. Jiao, Y. Li and J. Min, *J. Mater. Chem. A*, 2018, **6**, 15675-15683.
39. J. Min, X. Jiao, V. Sgobba, B. Kan, T. Heumüller, S. Rechberger, E. Spiecker, D. M. Guldi, X. Wan, Y. Chen, H. Ade and C. J. Brabec, *Nano Energy*, 2016, **28**, 241-249.
40. M. J. Newman, E. M. Speller, J. Barbé, J. Luke, M. Li, Z. Li, Z.-K. Wang, S. M. Jain, J.-S. Kim, H. K. H. Lee and W. C. Tsoi, *Sci. Technol. Adv. Mater.*, 2018, **19**, 194-202.
41. S. Li, Q. Ma, B. Qiu, L. Meng, J. Zhang, Y. Wu, Z. Zhang, Z.-G. Zhang and Y. Li, *Sol. RRL*, 2021, **5**, 2100515.
42. R. Cheacharoen, W. R. Mateker, Q. Zhang, B. Kan, D. Sarkisian, X. Liu, J. A. Love, X. Wan, Y. Chen, T.-Q. Nguyen, G. C. Bazan and M. D. McGehee, *Solar Energy Materials and Solar Cells*, 2017, **161**, 368-376.
43. Q. Zhang, B. Kan, X. Wan, H. Zhang, F. Liu, M. Li, X. Yang, Y. Wang, W. Ni, T. P. Russell, Y. Shen and Y. Chen, *J. Mater. Chem. A*, 2015, **3**, 22274-22279.
44. A. Armin, J. Subbiah, M. Stolterfoht, S. Shoae, Z. Xiao, S. Lu, D. J. Jones and P. Meredith, *Adv. Energy Mater.*, 2016, **6**, 1600939.
45. Z. Zhou, S. Xu, J. Song, Y. Jin, Q. Yue, Y. Qian, F. Liu, F. Zhang and X. Zhu, *Nat. Energy*, 2018, **3**, 952-959.
46. H. Tang, T. Xu, C. Yan, J. Gao, H. Yin, J. Lv, R. Singh, M. Kumar, T. Duan, Z. Kan, S. Lu and G. Li, *Adv. Sci.*, 2019, **6**, 1901613.

47. T. Xu, J. Lv, D. Zheng, Z. Luo, M. H. Jee, G. Ran, Z. Chen, Z. Huang, J. Ren, Y. Li, C. e. Zhang, H. Hu, T. Pauperté, W. Zhang, H. Y. Woo and C. Yang, *Energy Environ. Sci.*, 2023, **16**, 5933-5943.